Modelling ~~tides and storm surge~~extreme water levels using intertidal topography and bathymetry derived from ~~the waterline method applied to~~ multispectral satellite images

Wagner L.L. Costa[1], Karin R. Bryan[1], Giovanni Coco[2]

[1]School of Science, University of Waikato, 124 Hillcrest ~~road~~Road, E-F link, Hamilton, New Zealand.
[2]School of Environment, University of Auckland, Auckland, New Zealand.

Correspondence to: Wagner L.L. Costa (wc119@students.waikato.ac.nz)

Abstract. ~~Bathymetric~~Topographic and bathymetric data are essential for accurate predictions of flooding in estuaries~~,~~ because water depth ~~is a~~ and elevation data are fundamental ~~component in~~components of the shallow-water hydrodynamic equations used in ~~numericale~~e.g. models~~.~~ for storm surge and tides. Where LiDAR or in-situ acoustic ~~in-situ~~ surveys are unavailable, recent efforts have centred on ~~the use of~~using satellite images to ~~estimate~~derive bathymetry (SDB~~).~~) and topography (SDT). This work is aimed at (1) determining the accuracy of ~~SDB,~~SDT and (2) assessing the suitability of the SDT and SDB for surge/tidal modelling of estuaries. The ~~SDB is~~SDT was created by extracting the waterline as it tracks over the ~~bathymetry~~topography with changing tides~~, and is~~. The method was applied to 4 different estuaries in New Zealand: Whitianga, Maketū, Ōhiwa and Tauranga ~~Harbour~~. Results show that the waterline method provides similar ~~bathymetries~~topography to the LiDAR with a root-mean ~~-~~squared error equal to 0.2 m, and it is slightly improved when two ~~proposed~~ correction methods are applied to the ~~bathymetry~~topography derivations: the ~~removing~~removal of statistical bias (~~by 2cm~~2 cm improvement) and hydrodynamic modelling correction ~~(by~~ of waterline elevation (1 cm improvement). Finally, the use of ~~SDB~~SDT in numerical simulations of surge levels ~~is~~was assessed for Tauranga Harbour ~~with 4~~in four different scenarios that explore ~~the use of SDB in comparison~~different ways of incorporating the SDT compared to ~~bathymetry~~modelling using topographic data collected using non-satellite survey methods. One of these ~~includes the well-known Stumpf-ratio method to extract the SDB of~~ scenarios trials replacing the subtidal ~~regions~~bathymetry with SDB, derived using the well-known ratio-log method (so that only satellite information is used~~). The use of the satellite derived bathymetry~~ in surge modelling). For Tauranga Harbour, using SDT and SDB in hydrodynamic models does not result in significant differences in ~~terms of~~predicting high water levels~~,~~ when compared with the scenario modelled using surveyed bathymetry.

1 Introduction

~~Coastal flooding events have become increasingly concerning because of growing storm intensity (Emanuel, 2005; Sobel et al., 2016; Webster et al., 2005) and sea-level rise, which will potentially increase the risk exposure of coastal communities (Nicholls and Cazenave, 2010; Oppenheimer et al., 2019). In practice, predicting flooding events depends on understanding~~

~~the contribution from the astronomical tide, wave run-up, fluvial discharge, vertical land motion, and changes in the sea-level. In coastal zones, these processes can interfere in each other such as in, for instance, the tide-surge interactions (Spicer et al., 2019; Wankang et al., 2019; Zheng et al., 2020). In the specific case of estuaries, bathymetric data are essential for predictions (Cea and French, 2012; Parodi et al., 2020; Pedrozo-Acuña et al., 2012) because water depth is a fundamental component in the shallow-water hydrodynamic equations used in surge modelling. Water depth controls the amplitude and phase (timing) of the propagating tide as well as the estuary's geometry and length (which can cause shoaling and choking) and bed-shear stress (which reduces energy due to its effect on friction). The estuary's bathymetry is also fundamental for studying the tidal response to sea-level rise (Du et al., 2018).~~

~~Techniques to measure bathymetry in shallow water have evolved rapidly (Jawak et al., 2015). Acoustic techniques (e.g. echo-sounders) are known to produce highly-accurate data; however, such methods are constrained by cost, inaccessibility of remote areas, and environmental conditions in shallow water and estuaries (e.g. water turbidity, low tide navigational restrictions). To overcome these issues, efforts have centred on using spaceborn remote sensing (RS) techniques (Bishop-Taylor et al., 2019; Bué et al., 2020; Caballero and Stumpf, 2019), and there are several RS techniques to estimate bathymetry, each one of them having its own advantages/disadvantages and accuracy depending on the environment in which they are applied and its depth range (Gao, 2009). In comparison to acoustic techniques, RS methods are faster and applicable to a wider range of environments, including remote and/or shallow coastal waters (Caballero and Stumpf, 2019; Ehses and Rooney, 2015; Lyzenga, 1985), and allow bathymetry to be estimated over extensive areas which would not be accessible using traditional methods (Bishop-Taylor et al., 2019).~~

~~For shallow waters, between 0-30m depths, some SDB methods (Caballero and Stumpf, 2019; Stumpf et al., 2003) use a radiometric approach, which uses the property that different wavelengths are attenuated to varying degrees in the water column. In these cases, an empirical formula is used to fit the relationship between the ratio of reflectance of different spectral bands (resolved on a pixel-by-pixel basis) to the measured in-situ water depth. However, limitations include: the requirement of in situ bathymetric data to calibrate the empirical relationships; the decline in performance caused by variation in the benthic substrates and the inherent optical properties (IOPs) such as water turbidity and bottom reflectance, often occurring in enclosed seas, bays and estuaries (Morris et al., 2007). Novel techniques using physically based algorithms such spectral optimization algorithm (SOA) (Lee et al., 2011; Lyzenga et al., 2006; Wei et al., 2020) and methodologies to correct the water turbidity (Caballero and Stumpf, 2020) have been developed to solve the empirical model's limitations. Bué et al., 2020 proposed a technique that generates high density bathymetric data for intertidal zones by using a logistic regression equation to fit reflectance in the near infrared band (NIR) of multispectral images to the observed tide.~~

~~Another SDB method that is particularly appropriate for intertidal zones, the waterline method, has been widely applied to Synthetic Aperture radar - SAR (Catalao and Nico, 2017; Huang et al., 2001; Mason and Davenport, 1996) and multispectral (Khan et al., 2019) images. This method functions by detecting the land-water boundary in an image, and associating this line to the tidal height observed at the time of the image acquisition. The tidal height can be predicted by a regional tide model (Bishop-Taylor et al., 2019; Khan et al., 2019) or from a local tide gauge (Mason et al., 1997). The waterlines are mapped over~~

~~a number of images (each acquired at a different tidal level), and the resulting collection of waterlines is interpolated in the intertidal domain, generating a digital elevation model (DEM). The approach assumes that estuary morphology is constant throughout the period of image acquisition. The main disadvantages of this method are: the low number of estimated waterlines due to a reduction in the number of available images as consequence of cloud coverage; the dependency of accuracy on the number of processed images; the negative influence of bathymetric slope and complexity on waterline coverage; and, in the case of SAR images, the sensitivity of the sensors to windy conditions; i.e. changes in the backscatter signal due to the increased rugosity caused by the strong wind blowing in the water surface (Liu et al., 2013; Mason et al., 2001).~~

~~As SDB techniques have developed, cloud computation and storage systems such as Google Earth Engine (Gorelick et al., 2017) have advanced considerably, enhancing the capacity to easily manage large geographical datasets, which has allowed global-scale studies in coastal science to evolve rapidly. For instance, databases now exist on the distribution and changes to global tidal flats (Murray et al., 2019) as well as a global estimation of coastline position (Vos et al., 2019). Combining recent SDB methods and innovative cloud data storage and computation, extensive databases of satellite images can be quickly and easily processed, enabling bathymetry for multiple estuaries to be estimated routinely.~~

~~Despite the wide and growing application of SDB methods, it is not yet clear whether the accuracy of the resulting bathymetry is suitable for coastal tidal or storm surge modelling, both critical to managing adaptation to sea level rise. Only limited studies exist in related to the use of SDBs in numerical modelling, such as data assimilation in a coastal morphodynamic model (Mason et al., 2010). Our study is aimed at: (1) determining whether satellite imagery can be used to extract accurate intertidal bathymetric data; and, (2) assessing the use of the SDB for hydrodynamic modelling of estuaries.~~

~~2 Methods~~

~~The method was divided into 2 main steps, Figure 1: (1) the SDB estimation (using the waterline method and, for Tauranga Harbour only, the Stumpf-ratio method); and (2) the hydrodynamic modelling assessment. In addition, as part of step 1, two methods were trialled to remove a bias highlighted by a comparison to LiDAR observations (symbolised by the red and green fonts in Figure 2).~~

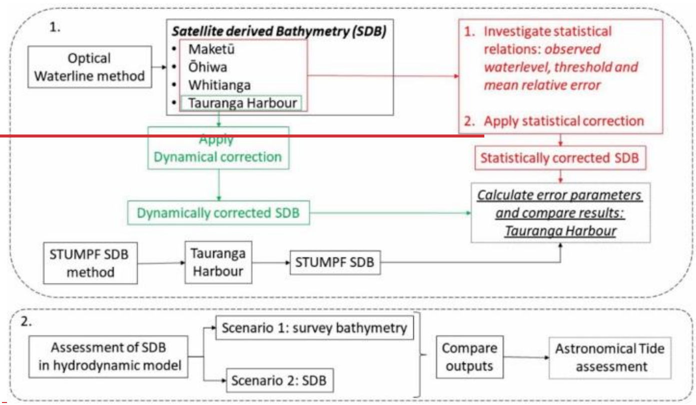

Coastal flooding has become increasingly concerning because of growing storm intensity (Emanuel, 2005; Webster et al., 2005; Sobel et al., 2016) and sea level rise, which will potentially increase the risk exposure of coastal communities (Nicholls and Cazenave, 2010; Oppenheimer et al., 2019). In practice, predicting flooding depends on understanding the contribution from the astronomical tide, storm surge, wave run-up, changes in the sea level and, in some cases, the fluvial discharge and vertical land motion. In coastal zones, these processes can interfere with each other, for example, in tide-surge interactions (Spicer et al., 2019; Wankang et al., 2019; Du et al., 2018). In the case of estuaries, bathymetric and topographic data are essential for coastal risk assessment (Parodi et al., 2020) because they influence the accuracy of water level predictions (Cea and French, 2012; Pedrozo-Acuña et al., 2012; Falcão et al., 2013; Mohammadian et al., 2022). Water depth is a fundamental component in the shallow-water hydrodynamic equations used in extreme water level modelling. Together with the estuary's geometry and length — which can cause shoaling and choking — and bed-shear stress — which reduces energy due to its effect on friction, bathymetry and topography control the amplitude and phase (timing) of the propagating tide. The estuary's morphology is also fundamental for studying the tidal response to sea level rise (Khojasteh et al., 2020, 2021; Du et al., 2018).

The methods used to measure bathymetry and topography in coastal zones have evolved rapidly. In estuaries, there are permanently inundated areas (which are generally shallow) and intertidal zones, which are areas flooded and exposed by the tide. Here we define the terms bathymetry and topography to reflect permanently-inundated and intertidal areas respectively. Currently, there are four types of systems for measuring these: ship-based systems (e.g., single-beam and multibeam echosounders), non-imaging active remote sensing (e.g. LiDAR), imaging active remote sensing (e.g. synthetic aperture radar — SAR), and imaging passive remote sensing (e.g. optical systems) (Jawak et al., 2015; Salameh et al., 2019; Ashphaq et al., 2021). Traditionally, the most commonly-used systems are echosounders and LiDAR. Both produce highly accurate data; however, several factors constrain their application, such as economic cost, staffing costs, inaccessibility of remote areas, and environmental conditions (e.g., low tide navigational restrictions). Consequently, approximately 70% of the world's coastal areas have not been surveyed or surveyed recently (IHO, 2020).

Space-borne remote sensing techniques overcome the limitations of traditional techniques and can provide topographic and bathymetric data for a wide range of environments, including areas that are more difficult to measure such as remote shallow coastal waters (Lyzenga, 1985; Ehses and Rooney, 2015; Caballero and Stumpf, 2019) and extensive intertidal areas (Bishop-Taylor et al., 2019; Fitton et al., 2021). Several methods are used to derive bathymetric data — hereafter called satellite-derived bathymetry (SDB) — in shallow waters (i.e., between 0–15m depth) using imaging passive remote sensing of reflectance (Ashphaq et al., 2021). Most of methods are developed around the process of light attenuation through the water column, and fall into two approaches. Empirical methods use direct observations of water depth in the study area to calibrate the reflectance-to-depth relationship (Stumpf et al., 2003; Caballero and Stumpf, 2019), and physics-based inversion algorithms use physical processes/models to solve for water depth (e.g., radiative transfer models) without the need for in situ calibration data (Lee et al., 1998, 1999; Kerr and Purkis, 2018).

In the present manuscript, we focused on empirical methods to obtain the SDB, and use the ratio-log method proposed by Stumpf et al. (2003). Its main limitations are the requirement of in situ bathymetric data for calibration and the sensitivity of the Stumpf method to environmental conditions that can change bottom and water reflectance — e.g., water turbidity and variation in the benthic substrates — that often occur in enclosed seas, bays and estuaries (Morris et al., 2021). Some studies have proposed techniques to tackle empirical issues (e.g., Caballero and Stumpf, 2020; Geyman and Maloof, 2019). Caballero and Stumpf (2020) have adjusted reflectance ratios to reduce the effects of water turbidity and calculated the maximum chlorophyll index first to identify pixels containing floating and submerged vegetation and then remove these pixels from further implementation of the ratio-log formula. Geyman and Maloof (2019) have implemented the cluster-based regression algorithm to deal with different bottom substrates, first segmenting the satellite image into zones of spectral homogeneity and then calibrating the log-linear colour-to-depth relationship separately for each class.

In intertidal regions, remote sensing can also be used to obtain satellite-derived topography (SDT) — and the waterline method is the most commonly applied. The method was first applied to SAR images (Mason and Davenport, 1996), and recently also to multispectral space-borne images (Khan et al., 2019; Salameh et al., 2020; Fitton et al., 2021). The technique functions by detecting the edge between the flooded and exposed intertidal zone in multiple images (i.e., the waterline) and assigning a height to each waterline by using the local tidal level at the time of image acquisition. The tidal level can be acquired by a numerical tide model (e.g., Khan et al., 2019; Kang et al., 2020; Salameh et al., 2020) or from a local tide gauge (Mason and Davenport, 1996; Salameh et al., 2020). The resulting collection of waterlines is interpolated over the intertidal domain, generating a digital elevation model (DEM). The approach assumes that estuary morphology does not change between images and has a gentle slope. The main disadvantages of this method are the dependence of accuracy on the number of images used in processing and the reduced performance in sites with complex morphology, i.e., variable terrain slopes within the intertidal zone (Liu et al., 2013; Salameh et al., 2019, 2020). Other methods used to derive topography in intertidal zones are the interferometric SAR (Li andGoldstein, 1990), satellite radar altimetry (Salameh et al., 2018) and near-infrared logistic approach (Bué et al., 2020).

As remote-sensing techniques have developed, cloud computation and storage systems such as Google Earth Engine (Gorelick et al., 2017) have also advanced considerably. Consequently, scientists now have an enhanced capacity to quickly manage large geographical datasets, allowing global-scale studies in coastal science to evolve rapidly (e.g., Murray et al., 2019; Vos et al., 2019; Bishop-Taylor et al., 2019). For instance, databases now exist on the distribution of and changes to global tidal flats (Murray et al., 2019), as well as a global estimate of coastline position (Almeida et al., 2021; Vos et al., 2019). Satellite-derived bathymetry (SDB) and topography (SDT) techniques are now routinely applied over extensive areas (e.g., Traganos et al., 2018; Bishop-Taylor et al., 2019; Fitton et al., 2021). Despite the vast and growing application of SDB and SDT methods to coastal science and engineering (Turner et al., 2021), it is not yet clear whether the accuracy of the resulting estimates is suitable for modelling extreme water levels in coastal areas (e.g., estuaries and bays). Only limited studies exist relating to SDB and SDT and numerical modelling — generally aimed at using the model to assign the waterline height (Khan et al., 2019; Salameh et al., 2020; Fitton et al., 2021). For instance, Mason et al. (2010) used SDT to calibrate a morphodynamical model.

Our study aims to evaluate whether SDT and SDB can replace surveyed data as a boundary condition in hydrodynamic modelling — focusing on predicting high water levels (surges and extreme high tides) in estuaries with complex morphology. We have three specific objectives:

1. To determine whether satellite imagery can be used to extract accurate SDT;
2. To investigate the main source of errors in the satellite-derived techniques; and,
3. To assess the use of SDT and SDB for hydrodynamic modelling of estuaries compared to data derived from traditional methods.

This manuscript is divided into two main parts, as illustrated in Figure 1: (a) the SDT and SDB framework and (b) the hydrodynamic modelling assessment. Firstly, we present the methods (Sect. 2), where we show the study sites and database (Sect. 2.1), the applied SDT and SDB methods (Sect. 2.2 and 2.3), and the specifications of the hydrodynamic modelling used in Sect. 2.5.2 and Sect. 2.6. Then we show the approaches we used to improve the SDT obtained using our framework (Sect. 2.5), how we assess the water level simulations using SDT and SDB (Sect 2.6), and how we assess our framework performance (Sect. 2.7). In Sect. 3, we show our results, the waterline-derived and the ratio-log-derived intertidal elevation (Sect. 3.1); the statistical and dynamical corrections (Sect. 3.2); the prediction of high water levels using SDT and SDB (Sect. 3.3). In Sect. 4, we discuss our main findings: the advantages and limitations of our proposed SDT and SDB framework and correction approaches (Sect.4.1 and 4.2); the comparison between SDTs derived from the waterline and ratio-log methods (Sect.4.3); the hydrodynamic modelling assessment (Sect.4.4); and, in Sect. 5, the conclusion.

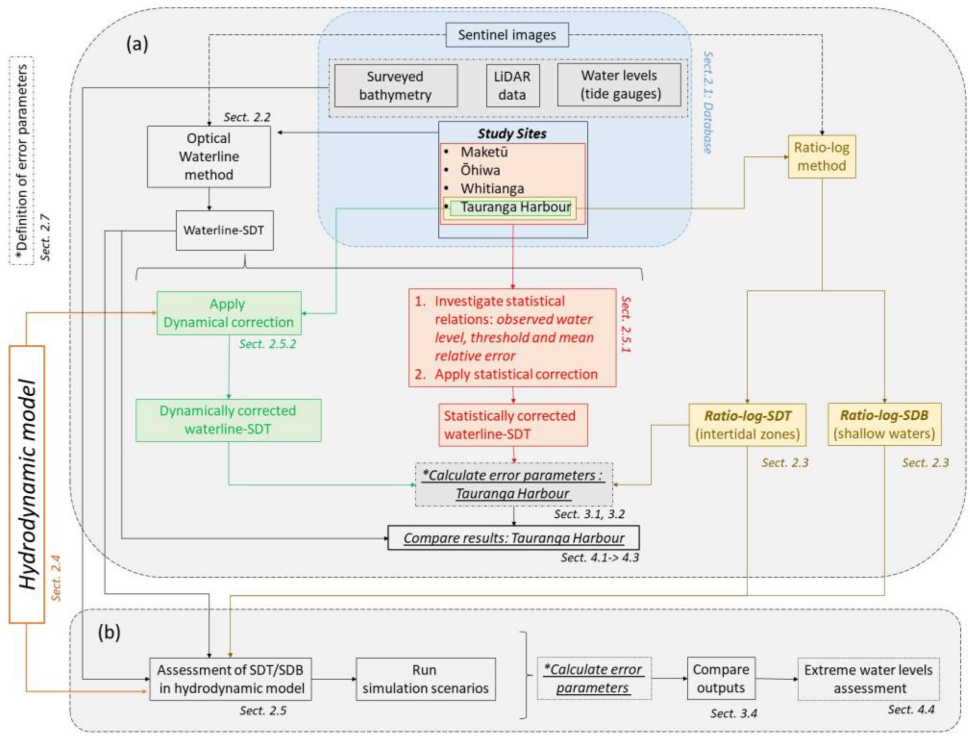

Figure 1: A flow chart showing the steps taken to derive the SDT/SDB (a) and to test its utility in modelling~~.~~ (b).

Formatted: English (New Zealand)

2 Methods

2.1 Study site and database

~~The study areas are four estuaries located in the east coast of Aotearoa New Zealand's North Island; three in the Bay of Plenty region: Tauranga, Ōhiwa and Maketū harbours and one in the Coromandel: Whitianga harbour, Figure 2A. The studied sites have microtidal regimes — the spring tidal range varies between 1.4 m to 1.9 m within estuaries – and all have wide intertidal areas covering from 58% to 84% of the estuaries' total area (Hume et al., 2016). For instance, the extent of the tidal flats is evident in Tauranga Harbour by comparing low (e.g. Figure 2B) and high (e.g. Figure 2C) tide images; the intertidal zone is~~

~~easily distinguished by the colour of sand accentuating reflectance in the near infrared band. Associated with tidal flats, mangrove forest can be observed in all the studied estuaries as well as vast seagrass banks for Maketū, Ōhiwa and Tauranga Harbour (the latter was studied in Ha et al., 2020).~~

~~For the implementation of SDB techniques, only tidal levels and imagery are needed. We used additional in situ bathymetric data to~~The study areas are four estuaries on the east coast of Aotearoa New Zealand's North Island. Three are in the Bay of Plenty region: Tauranga, Ōhiwa and Maketū harbours and one in the Coromandel: Whitianga harbour, Figure 2A. The studied sites have micro-tidal regimes — the spring tidal range varies between 1.4 m to 1.9 m within estuaries – and the equinoctial spring tides combined with severe storm surges drive the extreme sea levels (Rueda et al., 2019; Stephens et al., 2020). In New Zealand, the surges caused by storms usually add < 0.5 m to the water level, but the maximum surge ever registered was 2.29 m (Stephens et al., 2020). In Tauranga Harbour, the maximum storm-driven surge ever recorded is equal to 0.88 m (Stephens et al., 2020), and the tide can be attenuated by 10% to 17% (M2 component) when the tidal wave propagates through the estuary (Tay et al., 2013). The water level inside the study site estuaries is not considered to be substantially affected by the action of waves (i.e., wave set-up) because all of them are enclosed coastal lagoons with restricted entrances. All four estuaries have large intertidal areas covering from 58% to 84% of the estuaries' total area (Hume et al., 2016); see Table 1. The extent of the tidal flats is evident in Tauranga Harbour by comparing low (e.g., Figure 2b) and high (e.g., Figure 2c) tide satellite images. Mangrove forests can be observed in all the estuaries and seagrass banks are visible in Maketū, Ōhiwa and Tauranga Harbours (the latter was studied in Ha et al. (2020)). Detailed images of the intertidal zones in Tauranga Harbour and its seagrass banks and mangroves can be seen in Figure S3.

Imagery, tidal levels and topography data (e.g., LiDAR) were acquired to implement and validate the ~~SDB.~~SDT techniques. For the Bay of Plenty region, ~~the~~ historical tide levels were ~~extracted~~downloaded from the Bay of Plenty Council data portal ~~(https://envdata.boprc.govt.nz/);~~(https://envdata.boprc.govt.nz/); the ~~bathymetry~~topography data ~~consist~~consisted of the LiDAR survey for which a ~~1x~~ 1×1m resolution dataset was available on the Land Information New Zealand data portal ~~(https://data.linz.govt.nz/).~~(https://data.linz.govt.nz/). For Whitianga, we acquired ~~both~~ water level time series and elevation data (LiDAR) ~~by request~~ through the Thames-Coromandel District ~~Council's~~Council's website (http://www.tcdc.govt.nz/). The LiDAR data have ~~a vertical~~an accuracy of ± 0.2 m in the vertical and ± 0.6 m in the horizontal with 95% ~~of~~ confidence for the Bay of Plenty. ~~To calculate the SDB's accuracy, all~~All LiDAR data were converted to the local vertical datum (i.e., Moturiki 1953), which is 0.13 m below mean sea level (MSL), ~~by~~ using the GEOID elevation grids available in the LINZ data portal.

We used European Space Agency (ESA) Copernicus Sentinel satellite images accessed through Google Earth Engine ~~(Gorelick et al., 2017),~~(Gorelick et al., 2017) from spacecraft Sentinel 2A and B, product type level-2A. The Sentinel-2 products are composed of elementary tiles, which are ~~100x100~~100×100 km^2 ortho-images in the UTM/WGS84 projection, with a revisit frequency of 5 days in the Aotearoa New Zealand region. The level-2A product type provides bottom-of-atmosphere (BOA)

Formatted: English (United States)
Formatted: English (United States)
Formatted: English (United States)
Formatted: English (United States)
Formatted: English (United States)
Formatted: English (United States)
Formatted: English (United States)
Formatted: English (United States)
Formatted: English (United States)
Formatted: English (United States)
Formatted: English (United States)
Formatted: English (United States)
Formatted: English (United States)
Formatted: English (United States)
Formatted: English (United Kingdom)
Formatted: English (United Kingdom)
Formatted: English (United Kingdom)
Formatted: English (United Kingdom), Superscript
Formatted: English (United Kingdom)
Formatted: English (United Kingdom)
Formatted: English (United Kingdom)

images, which are already corrected for the effects of the top-atmosphere~~.~~, terrain and cirrus cloud using the Sen2Cor processing tool (ESA). Each image has the spectral resolution of 12 bands with spatial resolution differing between 10, 20 and 60 m depending on the band. Here we used the green (band 3, 560 nm), blue (band 2, 490 nm) and near~~-~~-infrared (band 8, 842 nm) bands, all of them with ~~10m~~10 m spatial resolution.

In summary, ~~for each estuary,~~ a complete set of LiDAR, tidal gauge observations and a satellite ~~images~~image was obtained for ~~this study~~each estuary. For example, the Tauranga Harbour dataset is shown in Figure 2: the location of the tide gauges (~~Omokoroa~~Ōmokoroa, Hairini and ~~Oruamatua~~Ōruamatua) and the intertidal exposure during low tide (Figure ~~2B~~2b) and high tide (Figure ~~2C~~2c), as well as their water level record for the acquisition period of the satellite images (Figure ~~2D). In the specific case of Tauranga Harbour, where a hydrodynamic model was run, additional bathymetric data was needed to supplement the SDB for the deepest parts of the model domain (e.g. tidal channels and coastal zone). The bathymetry data ("the multi-source bathymetry") used in the hydrodynamic model was assembled using a combination of data from multiple sources: Multibeam survey (Port of Tauranga, 2017), LiDAR (2008 from AAMHATCH and 2016 from LINZ) and LINZ hydrological charts NZ 5411, 2016. These were converted from chart datum (lowest astronomical tide) to mean sea level by adding a uniform value of 1.05m to the data.~~2d).

Formatted: English (United Kingdom)
Formatted: English (United Kingdom)
Formatted: English (United Kingdom)
Formatted: English (United Kingdom)
Formatted: English (United Kingdom)
Formatted: English (United Kingdom)
Formatted: English (United Kingdom)
Formatted: English (United Kingdom)
Formatted: English (United Kingdom)
Formatted: English (United Kingdom)
Formatted: English (United Kingdom)
Formatted: English (United Kingdom)
Formatted: English (United Kingdom)
Formatted: English (United Kingdom)

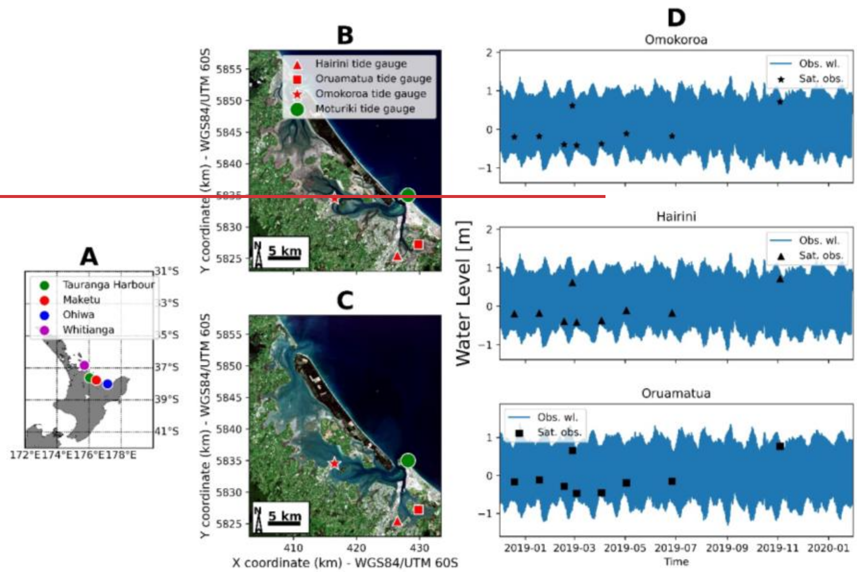
A
Tauranga Harbour
Maketu
Ohiwa
Whitianga
B
Hairini tide gauge
Oruamatua tide gauge
Omokoroa tide gauge
Moturiki tide gauge
5 km
C
Y coordinate (km) - WGS84/UTM 60S
X coordinate (km) - WGS84/UTM 60S
D
Omokoroa
Hairini
Oruamatua
Obs. wl.
Sat. obs.
Water Level [m]
Time

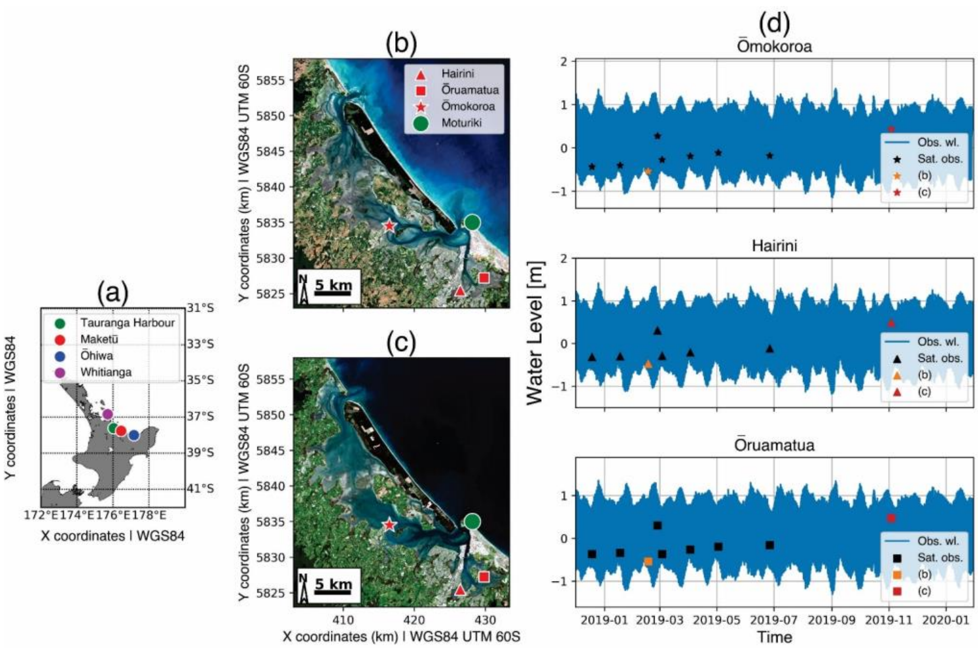

Figure 2 ~~Study sites.~~: The location of the four New Zealand estuaries where the ~~SDB~~SDT method was tested (~~A~~a). Tauranga Harbour and tide gauge locations during low tide (~~B~~b) and high tide (~~C).~~c) with the background image from ESA Sentinel 2A. Water level time series from the three of local tide gauges shown in panels b and c during the period over which satellite images were acquired (~~D). Background image: ESA Sentinel 2A.~~d). The water levels associated with images shown in panels b and c are marked with yellow and red symbols (Vertical Datum: MSL).

2.2 Satellite-derived ~~bathymetry techniques~~topography: the waterline method.

~~The process of generating the SDB in intertidal zones using the waterline method was composed of 4 stages. First, image pre-processing was done through the Google Earth Engine application (Gorelick et al., 2017) using the Google Colaboratory environment. In this step, for each estuary, a search was performed in the Copernicus database, for Sentinel 2A and B, product type level-2A, to extract an image collection where each image covers the estuary domain and is cloud-free. The number of images corresponding to each estuary's collection and environmental properties (e.g. coverage of intertidal zone in the estuary; spring tidal range) is shown in Table 1.~~

Our proposed framework to generate the SDT in intertidal zones using the waterline method (waterline-SDT) is composed of four stages, as illustrated in Figure 3: stage 1 is to query an image collection, stage 2 is to identify the intertidal zone, stage 3 is to determine the waterline position and height, and stage 4 is to post-process results. First, we acquired an image collection for each estuary through the Google Earth Engine application (Gorelick et al., 2017) using the Google Colaboratory environment. Each image collection has images from the satellite Sentinel 2A and B, product type level-2A, covering the estuary domain, in which less than 5% of the pixels are covered by clouds. We have allowed a certain number of images with low cloud coverage because of the restricted number of available images; however, any irregularities from the small areas of clouds and their shadows were removed manually in the post-process analysis. The number of images corresponding to the collection and environmental properties for each estuary (e.g., coverage of intertidal zone in the estuary; spring tidal range) is shown in Table 1.

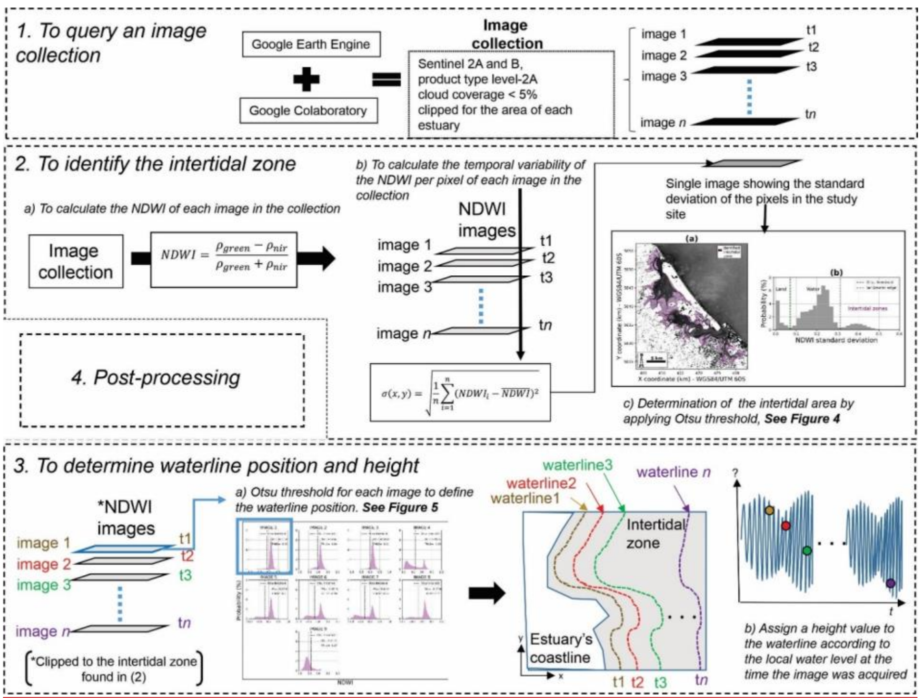

<u>Figure 3: Our proposed framework for application of the waterline method to derive topographic data in intertidal zones. NDWI is the index used to detect the existence of water from satellite reflectance (see text).</u>

Table 1 Number of images in the image collection for each estuary.

Estuary	*Nº of images in the collection*	*Total intertidal area* ~~(Hume et al., 2016)~~(Hume et al., 2016)	*Surface area* (Hume et al., 2016)	*Spring tidal range*
Tauranga Harbour	9	77%	~200.44 km^2	1.75 m
Ōhiwa	~~7~~6	84%	~27.00 km^2	1.9 m
Maketū	~~15~~12	58%	~ 2.64 km^2	1.4 m

Inserted Cells

Formatted Table

Whitianga	8	72%	*~ 15.50 km^2*	1.7 m

~~Second, we identify the intertidal zone by calculating the temporal variability at each pixel of the Normalized Difference Water Index (NDWI) over the entire image collection (McFeeters, 1996), using Equation 1:~~

To eliminate pixels that are not in the intertidal area (stage 2 in Figure 3) — thus avoiding needless image processing — we used the approach based on Bué et al. (2020). We identify the intertidal zone by calculating the temporal variability at each pixel of the Normalized Difference Water Index (NDWI) (McFeeters, 1996) over the entire image collection, using Equation 1:

$$\sigma(x, y) = \sqrt{\frac{1}{n}\sum_{i=1}^{n}(NDWI_i - \overline{NDWI})^2}; \qquad (1)$$

$$NDWI = \frac{\rho_{green} - \rho_{nir}}{\rho_{green} + \rho_{nir}};$$

where *x* and *y* are the pixel coordinates, *n* is the number of images in the collection, ρ_{green} and ρ_{nir} are the reflectance of the green and near~~-~~infrared bands of Sentinel-2 images, respectively. As a result, one single grey scale image is ~~produced~~generated representing the *NDWI* temporal standard deviation (σ), Figure ~~3. Since the NDWI in each pixel in the intertidal zone is expected to vary more because~~4(a). Because of the ~~constant~~consistent change between exposed (low tide) and inundated (high tide) conditions, we assume that the highest ~~values of~~ standard deviation values will occur in the intertidal zones. ~~To identify the tidal flat areas~~Thus, we ~~set~~ determine that the pixels representing the intertidal zone are the ones with an σ greater than a threshold ~~by~~ value — for Tauranga Harbour, the threshold is > 0.32, Figure 4(b). The threshold is set using the Otsu approach ~~(Nobuyuki Otsu, 1979).~~(Otsu, 1979), where its value depends on the probability distribution of σ in each image. The Otsu method identifies the optimum threshold between two data classes ~~of data~~ in the image distribution that maximizes the value of the within-class variance~~, defined as a weighted sum of variances of the two classes:~~

$$\cancel{\sigma_w^2(t) = \omega_0(t)\sigma_0^2(t) + \omega_1(t)\sigma_1^2(t);} \qquad \cancel{(2)}$$

~~where ω_0~~. The advantage of using an adaptive threshold is that we can objectively tailor the threshold to each image collection and ~~ω_1 are the probabilities of the two classes separated by threshold t, and σ_0^2 and σ_1^2 are the variances of these two classes. The intertidal zone identified for Tauranga Harbour is presented in Figure 3. A polygon is generated in order to mask the tidal flat in every image, avoiding needless image processing outside the intertidal area~~estuary.

Formatted: Font: Italic
Formatted: Font: Italic
Formatted: Font: Italic
Formatted: Font: Italic
Formatted: Font: Italic, Subscript
Formatted: Font: Italic
Formatted: Font: Italic, Subscript
Formatted: Subscript
Formatted: Font: Italic
Formatted: Font: Italic

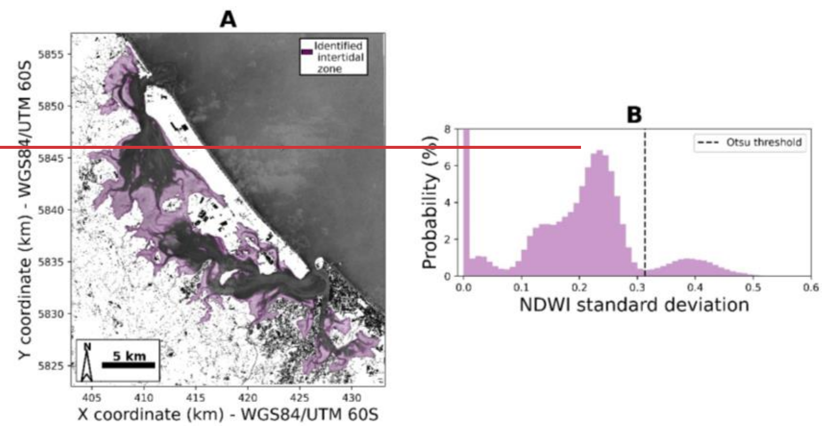

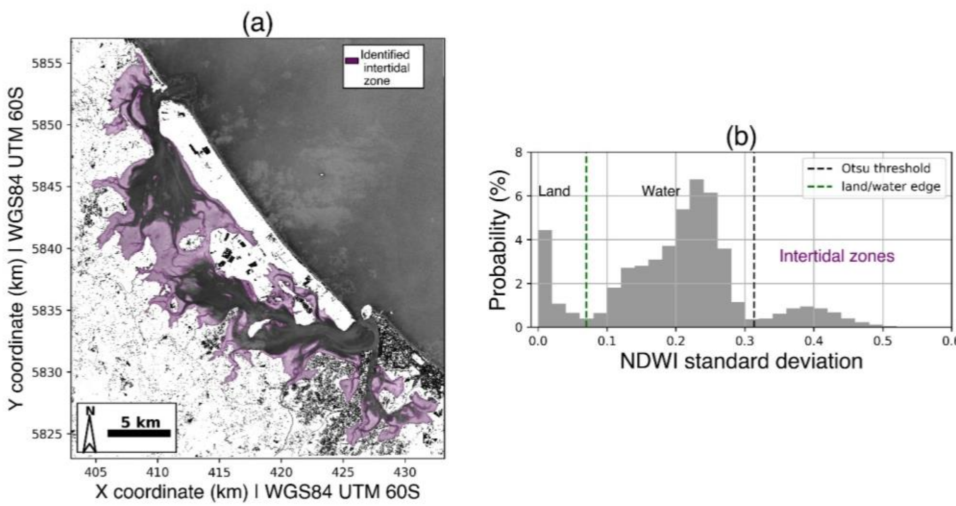

Figure 4~~: Identified intertidal areas. (A~~: (a) Intertidal areas identified using the temporal variability of *NDWI* ~~standard deviation from~~of the Tauranga Harbour image collection. Determination of the Otsu threshold for the identification of the intertidal zone (~~B~~b).

Formatted: Font: Not Bold

Formatted: Font: Italic

~~Third, the position of the waterline in each image is defined by applying the algorithm "Finding_Contours" from the scikit.measure (Van Der Walt et al., 2014) Python library. This contour extraction method searches for a given value (threshold) in a two-dimensional array of pixels, using the 'marching squares' algorithm (Lorensen and Cline, 1987) to identify precise~~

~~contour boundaries by linearly interpolating between adjacent pixel values. Again the adaptive Otsu threshold is used to find the location of the waterline from the NDWI maps for each image, Figure 4.~~

~~Fourthly, once the waterline for a given image is identified, a height value is assigned to it accordingly to the corresponding tide level observed at the closest tide gauge (Omokoroa for the Tauranga Harbour case study, Figure 2D).~~

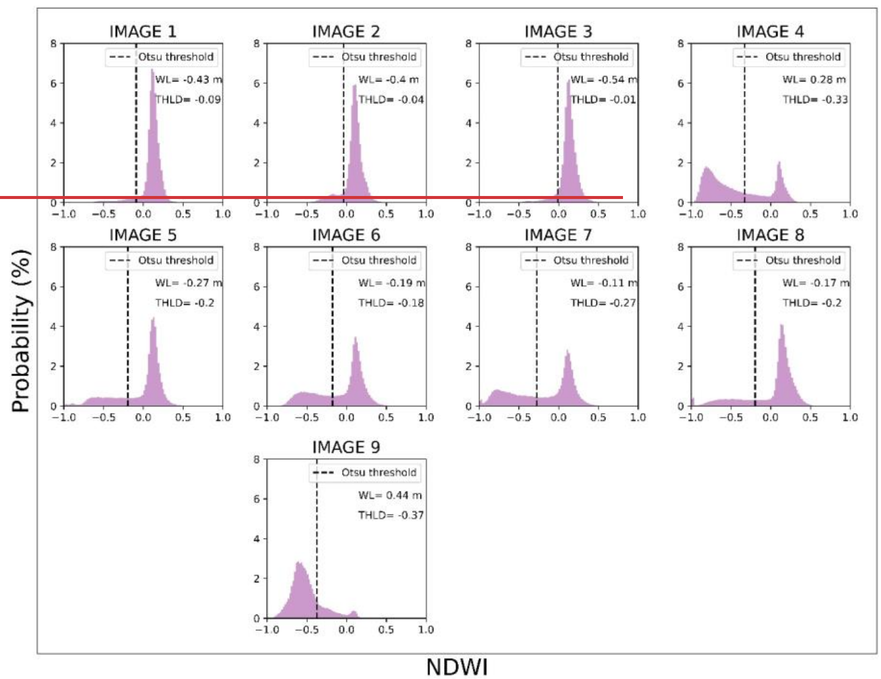

In the third stage (Figure 3) for each image in the collection, we clipped the corresponding *NDWI* maps into the intertidal zone (which was defined using the whole image collection in stage two). From the intertidal *NDWI* maps, the waterline position in that image was extracted by applying the algorithm "Finding_Contours" from the scikit.measure (Van DerWalt et al., 2014) Python library. This contour extraction method searches for a given value (threshold) in a two-dimensional array of pixels, using the 'marching squares' algorithm (Lorensen and Cline, 1987) to precisely identify contour boundaries by linearly interpolating between adjacent pixel values; therefore, the method is able to define waterline with a subpixel resolution. We used Otsu method to determine the threshold that should be applied to each image; Figure 5 shows the distribution of *NDWI* for each image in the Tauranga collection. Once we identify the waterline for a given image, we assign a height value to it by finding the corresponding observed tide level at the local tide gauge (Ōmokoroa for the Tauranga Harbour case study, Figure

2D). After we have processed all images in the collection, several waterlines with different height values are created (see Figure 3, stage 3b), which can be gridded to create the waterline-derived-STD (hereafter the "waterline-STD"). We assessed the accuracy of the SDT against the LiDAR data by comparing the waterline sample-by-sample and the corresponding digital elevation model (DEM). We used the module DELFT-QUICKIN to create DEMs for each estuary. The triangular interpolation method was applied in a grid with a spatial resolution of 10 m.

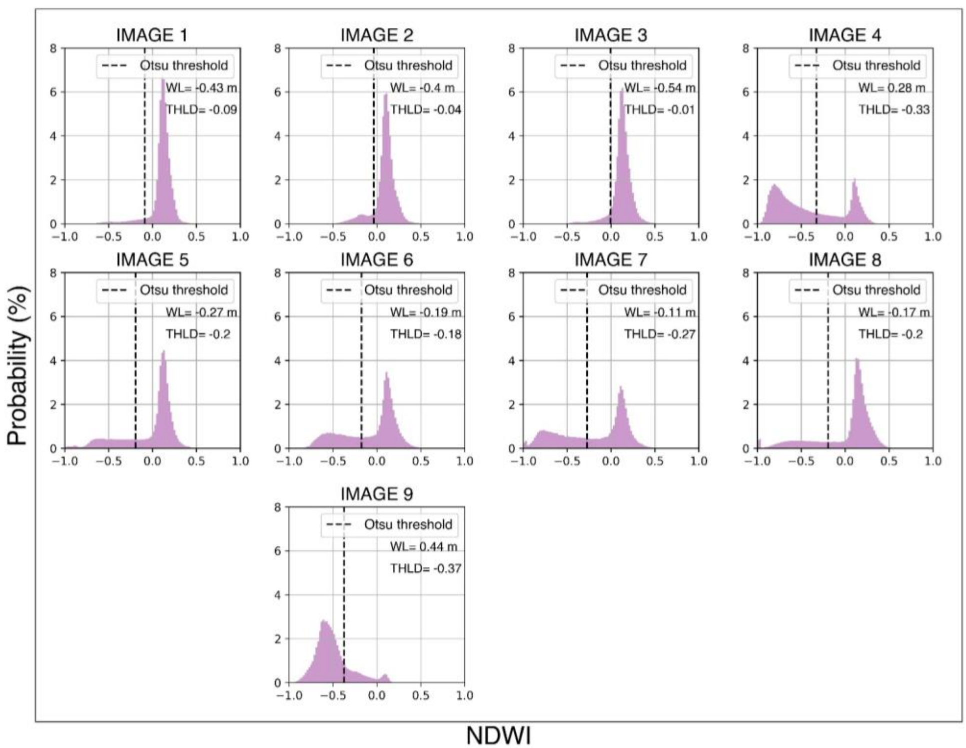

Figure 5: Otsu threshold (THLD) applied to identify the waterline ~~coordinate points~~position for each image in the Tauranga Harbour ~~image~~ collection. The observed water level from the ~~Omokoroa~~Ōmokoroa tide gauge at the moment of the image acquisition (i.e., waterline height relative to mean sea level) is also shown in each panel (marked WL).

Formatted: Font: Times New Roman

2.3 Satellite-derived bathymetry: the ratio-log method.

Additionally, the ratio-log method (Stumpf~~-ratio method (Stumpf et al., 2003)~~ et al., 2003) was applied in Tauranga Harbour separately for intertidal zones (ratio-log-SDT) and shallow water (ratio-log-SDB) (the ratio-log-SDT is used in the comparison of methods in Part (a), Figure 1 and ~~deeper areas separately. In the first case it was~~ both the SDT/SDB are used in the assessment of modelling in Part (b), Figure 1). Originally, the ratio-log empirical approach has been used to ~~compare with the waterline-SDB;~~derive shallow water bathymetry. However, because of the relative low turbidity of intertidal water in Tauranga Harbour, we hypothesized that the method could be suitable also for deriving topography on intertidal zones. We applied the method to an image acquired at high tide, where the intertidal zone was completely flooded.

In the Part 2 of the study, we use the SDT and ~~in the second case, to use~~ SDB in the hydrodynamic modelling ~~— following Costa et al., (in press),~~(building on a pilot study in Costa et al. (2021)), where the method was trialled in a sub-estuary of Tauranga Harbour~~— detailed~~). Detailed information about the application of the ratio-log method and the ~~estimates~~results for tidal flats and shallow water are provided in Supplement A~~ and Figure S1~~, Figure S1 and Figure S2. Because the method is based on an empirical fit, additional bathymetric data are needed to implement the ratio-log method for shallow water. For this, we used the multiple-source bathymetric data detailed in Sect. 2.4.

2.~~3 Assessment of framework performance~~

~~We assessed~~4 Hydrodynamic modelling; the ~~accuracy of the SDB and hydrodynamic model performance by calculating the following error metrics: root mean square error (RMSE), maximum absolute error (MAE), relative error (RE), coefficient correlation (R2), and bias (BIAS) (Eq. 3–7 respectively). In the corresponding equations, h~~$_{est}$ ~~is the estimated value (e.g. SDB, hydrodynamic model output) and h~~$_{obs}$ ~~is the observed value (e.g. LiDAR data, tide gauge measurements). In the case of SDB evaluation, its relative error can be either negative or positive, when the SDB is shallower or deeper than the LiDAR data, respectively. For illustrating this calculation, a schematic is in Figure 5, showing that although the error is evaluated in terms of height differences, it can arise because of either horizontal or vertical inaccuracies.~~baseline model

$$\cancel{RMSE = \sqrt{\sum_{i=1}^{n} \frac{(h_{est} - h_{obs})^2}{n}};} \quad (3)$$

$$\cancel{MAE = \max_{i=1 \ldots n} |h_{est}i - h_{obs}i|;} \quad (4)$$

$$\cancel{RE = h_{obs} - h_{est};} \quad (5)$$

$$\cancel{R^2 = \frac{\sum_{i=1}^{n} (h_{est}i - \overline{h_{obs}})^2}{\sum_{i=1}^{n} (h_{obs_i} - h_{est_i})^2 + (h_{est_i} - \overline{h_{obs}})^2};} \quad (6)$$

$$\cancel{BIAS = \overline{h_{est}} - \overline{h_{obs}};} \quad (7)$$

Formatted: Font: Bold

Formatted: English (United Kingdom)

Formatted: Heading 2

Formatted: English (United Kingdom)

Formatted: Font: 10 pt

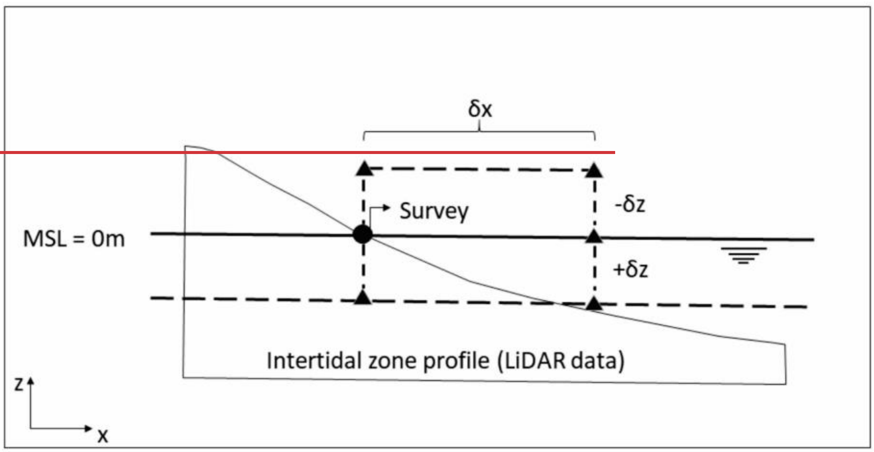

~~**Figure 5: Schematic showing the error calculation where the circle shows the actual location of the water line, and triangles show the location of the remotely sensed shoreline. There are two ways that an error can be caused. The waterline can be detected landward or seaward of its actual location (δx), or the waterline is assigned an elevation that is too high or too low (δz).**~~

~~**2.4 The SDB correction approaches**~~

~~The accuracy of the waterline SDB method can be limited either by environmental conditions that affect the ability to correctly identify the shoreline — e.g. complexity of the intertidal zone's morphology, presence of seagrass, groundwater seepage leaving a film of moisture on the exposed intertidal (Huisman et al., 2011) — and spatial changes to the tide level, caused by the propagation of the tide through the Harbour. These effects meant that consistent bias in the elevation of the SDB relative to LiDAR were detected. Two different correction methods were tested to improve the SDB: the statistical and the dynamical correction.~~

~~The statistical correction is based on the dependence of the bias on the value of the Otsu threshold (THLD) during each image acquisition, in all the studied estuaries. This correction was developed on the basis that the detected waterline is further seaward or landward of the actual waterline. The dynamical correction assumes that the bias was generated because the water level is higher or lower than the actual waterline, and was developed using a hydrodynamic model to simulate the astronomical tide propagation through the Tauranga Harbour. The model used was the DELFT3D FLOW, and the domain and bathymetry are shown in Figure S3 (Supplement B), covering the centre to southern part of the Harbour with a 20x20 m resolution grid. The open boundaries were set as free Neuman boundaries in the north and south and the astronomical components were used to force the water level along the seaward boundary. For the latter, harmonic astronomical tidal analysis was undertaken on the Moturiki Island tide gauge using U_tide (Codiga, 2011).~~

A baseline hydrodynamic model was set up for Tauranga Harbour. We only applied the modelling study to this estuary because it has already a previous model calibrated and validated for the bed roughness (following Stewart (2021)).The purpose of the baseline model was first to correct the waterline-SDT by accounting for the tidal propagation within the estuary (Sect. 2.5.2); the second was to assess the use of SDT and SDB as a boundary condition in modelling extreme water levels in estuaries (Sect. 2.6). We used the model DELFT3D-FLOW for this task. The grid domain and interpolated bathymetry are shown in Figure S4 (Supplement B), and they cover the central to the southern part of the Harbour with a 20×20 m resolution grid. We set the north and south boundaries as open boundaries (free Neuman), and we forced the water level along the seaward boundary with the astronomical components of the tide. For the latter, harmonic astronomical tidal analysis was undertaken on the Moturiki Island tide gauge using U_tide (Codiga, 2011). The topographic and bathymetric data used in the hydrodynamic model were assembled using a combination of data from multiple sources: Multibeam survey (Port of Tauranga, 2017), LiDAR (2008 from AAMHATCH and 2016 from LINZ) and LINZ hydrological charts NZ 5411, 2016. These data were all converted to mean sea level (MSL) vertical reference.

The model was validated to ensure the bed roughness parameters were appropriate by simulating an equinoctial tidal period~~,~~ from 01/03/2019 to 31/03/2019. The details of the model setup, calibration and validation are presented in Supplement B. The vertical datum in the simulation was the ~~mean sea level (~~MSL~~),~~, and the time step~~ used~~ was 0.5 min; the advection scheme for calculating the flooded and dried cells is cyclic, using the water level averaged on the grid cells. ~~The ~~We calibrated the model ~~performance was assessed ~~against three tide gauge ~~observations~~observation points (~~Omokoroa~~Ōmokoroa, Hairini and ~~Oruamatua) using the RMSE, MAE and R2 (see Sec. 2.3 for explanations).~~Ōruamatua). The model ~~shows good approximation to~~approximates the predicted data~~, with RMSE varying between 6 and 8 cm, and maximum error (MAE) within 21–26 cm and a correlation (R2) of 0.98 at the three observation points, Figure S4 (~~ well (shown in Supplement B).

Formatted: Font: Bold

~~Ideally, to be able to use the SDB methods for sites where there is no LiDAR coverage, we need a dynamical correction that only uses the SDB to assess the propagation of the tidal wave. After validating the bed roughness, the intertidal bathymetry in the model was replaced by the SDB — which was previously converted from local datum (Moturiki 1953) to MSL by adding 13 cm to its value — using the Delft3D- QUICKIN tool. Using this new depth file, simulations were done for the time period during which each of the 9 images in the image set were acquired. Each case had a simulation period corresponding to the ten-day period prior to the date and time of acquisition of the satellite image. Finally, each point along the satellite-detected waterline was assigned a height value by interpolating the water level model output for the time that correspond to the moment the images were acquired by the satellite.~~

~~2.5~~2.5 The SDT correction approaches

2.5.1 Correcting SDT using the bias between LiDAR data and SDT: the statistical correction

The accuracy of the waterline SDT method can be limited by environmental conditions that affect the ability to correctly determine the waterline at different tide levels within the tidal flats and at the boundary between shallow water and intertidal zones. — e.g., the complexity of the intertidal zone morphology, water turbidity and variation of the benthic substrates. All estuaries that we studied have similar environmental conditions; for example, the complexity of the morphology (they are all barrier-enclosed estuaries with channelization), the white-sand substrate, the presence of seagrass, and the groundwater seepage can be potential sources of error in topographic data estimates. Groundwater seepage leaves a film of moisture on the exposed intertidal detectable in images (Huisman et al., 2011). Therefore, a statistical correction was developed on the basis that the detected waterline is consistently further seaward or landward than the actual waterline because of these environmental conditions. For the statistical correction, we fitted a linear equation between the value of the Otsu threshold — used to positioning the waterline within the intertidal zone (see Sect. 2.2) — and the bias between the waterline-SDT and the LiDAR data in all the estuaries we studied. The statistical correction removed the bias.

2.5.2 Correcting SDT using hydrodynamic model: the dynamical correction

When a tidal wave propagates inside an estuary, it can experience wave deformation such as shoaling, reflection and dampening, which implies, together with the time it takes for the tide to propagate around a large estuary, that the water level is not homogeneous throughout the estuary at one instant in time. Thus, when considering a water level recorded in a single tide gauge to assign height values to a waterline, our estimates can be higher or lower than the actual waterline elevation. To correct the waterline-SDT (Sect. 2.2) for the tidal propagation, we used a hydrodynamic model (Sect. 2.4); this correction approach is hereafter called dynamical correction, and we implemented it as follows.

First, we replace the model bathymetry in the intertidal zones with the statistically-corrected waterline-SDT. We retained the original bathymetry in the shallow water areas and created a new depth file. Using this new depth file, we performed nine independent simulation cases corresponding to the nine images in the Tauranga image collection. Each case had a simulation period corresponding to the ten days prior to the date and time that the satellite image was acquired to ensure that initial conditions were no longer important. We then associated each of the spatially-varying waterlines (determined as described in Sect. 2.1) with the corresponding spatially-varying water level model output, using interpolation to extract collocated water levels from the gridded model output. As a result, the water levels of each waterline extracted from each image varied spatially rather then set to a constant — as is the case of the waterline-SDT derived according to Sect. 2.2.

2.6 Assessing water level simulations with SDB and SDT

~~To~~We developed four different simulation scenarios to evaluate the accuracy of hydrodynamic simulations using SDB and SDT against the use of our existing model bathymetry which was created with LiDAR, multibeam and echo-sounder data (‘surveyed bathymetry ~~data, we developed 4 different simulation scenarios (~~’ in Table 2). ~~The~~ The latter is our baseline model, S1 ~~is the validated model specified~~, and was described in Sect. 2.4~~, that uses the multi-source survey bathymetry (i.e. LiDAR, multibeam, digitalised nautical charts) throughout the model domain; this base case represents the “usual” situation~~. The S1 scenario simulates when the modeller depends only on the in situ measured bathymetry. In the S2 and S3 scenarios, we replaced the intertidal zone bathymetry with the SDT generated by using the waterline (waterline-SDT) and ~~Stumpf-derived SDB~~the ratio-log (ratio-log-SDT) methods, respectively~~, to evaluate which technique would be the best replacement for multi-source data in the tidal flat area.~~. The S4 scenario was developed to assess the use of ~~wholly~~ only SDB ~~derived bathymetry~~and SDT in the entire model domain~~. For that,~~ (so only satellite-derived data). We use the waterline-~~derived SDB is used~~SDT in the tidal flat and the ~~Stumpf-derived~~ ratio-log-SDB ~~is used in~~for the ~~deeper~~shallow areas ~~inside~~within the harbour. To assess the simulations, we compared the water level prediction made by each scenario against water level observations at the three ~~observation~~ points (~~Omokoroa~~Ōmokoroa, Hairini, and ~~Oruamatua~~Ōruamatua) and the water level output maps ~~in~~from each simulated scenario in terms of RMSE, ~~MAE~~MAXE, and R2. Other configurations applied to the scenarios (i.e., time period, time step, forcing conditions) are the same as described in Sect. 2.4.

Table 2 - Simulation scenarios to assess the use of SDT and SDB in hydrodynamic modelling.

Scenarios	Source intertidal zone	Source ~~deeper areas~~shallow waters
S1	surveyed bathymetry	surveyed bathymetry
S2	waterline-~~derived SDB~~SDT	surveyed bathymetry
S3	~~Stumpf-derived SDB~~ratio-log-SDT	surveyed bathymetry
S4	waterline-~~derived SDB~~SDT	~~Stumpf-derived~~ Ratio-log-SDB

2.7 Assessment of framework performance

We assessed the accuracy of the SDB, SDT, the hydrodynamic model, and the dynamical and statistical corrections by calculating the following error metrics: root mean square error (RMSE), maximum absolute error (MAXE), relative error (RE), coefficient correlation (R2), and bias (BIAS) (Eq. 3–7 respectively). In the corresponding equations, h_{est} is the estimated value (e.g., SDT, SDB, hydrodynamic model output), and h_{obs} is the observed value (e.g., LiDAR data, tide gauge measurements). In the case of SDB and SDT evaluation, its relative error can be either negative or positive when the SDB/SDT is shallower

Formatted: English (New Zealand)

or deeper than the LiDAR or surveyed data, respectively. For illustrating this calculation, a schematic is provided in Figure 6, showing that although the error is evaluated in height differences, it can arise because of either horizontal or vertical inaccuracies.

$$RMSE = \sqrt{\sum_{i=1}^{n} \frac{(h_{est} - h_{obs})^2}{n}}; \qquad (3)$$

$$MAXE = \max_{i=1 \dots n} |h_{est}\,i - h_{obs}\,i|; \qquad (4)$$

$$RE = h_{obs} - h_{est}; \qquad (5)$$

$$R^2 = \frac{\sum_{i=1}^{n} (h_{est}\,i - \overline{h_{obs}})^2}{\sum_{i=1}^{n} (h_{obs_i} - h_{est_i})^2 + (h_{est_i} - \overline{h_{obs}})^2}; \qquad (6)$$

$$BIAS = \overline{h_{obs}} - \overline{h_{est}}; \qquad (7)$$

Formatted: Font: 10 pt

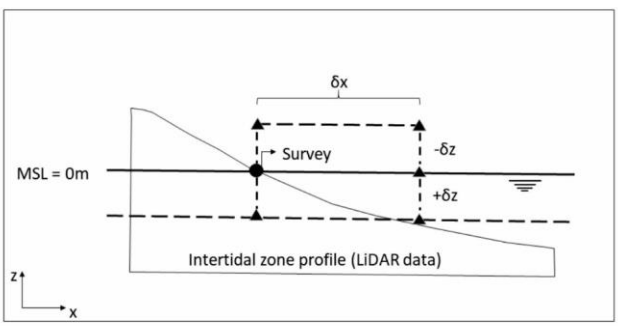

Figure 6: Schematic showing the error calculation. The circle shows the actual location of the water line, and triangles show the location of the remotely sensed shoreline. There are two ways that an error can be caused. The waterline can be detected landward or seaward of its actual location (δx), or the waterline is assigned an elevation that is too high or too low (δz).

3 Results

3.1 The waterline satellite derived ~~bathymetry~~topography (waterline-SDT)

The waterline ~~SDB~~ SDT accuracy, compared to the LiDAR data, for all the studied estuaries, is shown in ~~Table 3;~~Table 3; the average ~~error was 0.28 m and 1.58 m~~ RMSE across all estuaries~~, for RMSE~~ was 0.33 m, and ~~MAE respectively~~the average MAXE was 1.74 m. The technique's worst performance was in ~~Ōhiwa~~the Maketū estuary (RMSE =0.~~35~~41 m and ~~MAE~~MAXE= 2.38 m), Figure ~~S5, probably due to its complex morphology (i.e. wide intertidal zones, complex narrow channels and irregular bathymetry).~~ S6. Ōhiwa and Whitianga estuary~~, Figure S6, had a similarly higher error for the same reasons. In addition, the length and elongated geometry of Whitianga estuary — 8 km from the mouth to the inner part where~~

~~the intertidal zone was detected — can amplify errors related to tide wave propagation. Despite their different dimensions,~~ have similar performances, Figure S5 and S7. Tauranga Harbour ~~and Maketū (the latter in Figure S7) have similar performance, probably due to similar water optical properties (i.e. water colour, bed colour, infrared and green bands) and similar bathymetric slopes.~~is associated with the best estimates with RMSE = 0.20 m. Note that the error parameters calculated for the corresponding DEMs show lower errors, especially in terms of MAXE. The details about the images that were acquired and the corresponding water level for each estuary is shown in Supplement C.

Table 3 Waterline-~~derived SDB~~SDT errors for every studied estuary. DEM is the digital elevation model obtained by interpolating the corresponding waterline-SDT in the intertidal zone with spatial resolution of 20m and triangulation method. The elevation range in the LiDAR data within the intertidal zone is also shown. Vertical Datum: MSL.

~~*Estuary*~~	~~*RMSE*~~	~~*MAE*~~	~~*R2*~~
~~*Ōhiwa*~~	~~0.35~~	~~2.00~~	~~0.90~~
~~*Whitianga*~~	~~0.35~~	~~1.00~~	~~0.97~~
~~*Maketū*~~	~~0.22~~	~~1.75~~	~~0.93~~
~~*Tauranga Harbour*~~	~~0.20~~	~~1.60~~	~~0.86~~
~~*Average*~~	~~0.28~~	~~1.58~~	~~0.91~~

	SDT		***DEM***		***LiDAR***
Estuary	***RMSE (m)***	***MAXE (m)***	***RMSE (m)***	***MAXE (m)***	***elevation range (m)***
Maketū	0.41	2.38	0.47	2.19	-0.63 | +1.90
Ōhiwa	0.35	2.00	0.34	1.61	-0.98 | +2.98
Tauranga Harbour	0.20	1.60	0.23	1.14	-1.11 | +1.44
Whitianga	0.35	1.00	0.28	1.17	-1.12 | +1.92
Average	0.33	1.74	0.33	1.53	

Although the ~~SDB~~SDT accuracy differs depending on the estuary, ~~the mean relative error (MRE) is strongly linearly-correlated with the observed water level (Z) and the Otsu adaptive threshold (THLD), as shown in Figure 6. The THLD and Z correlation (R2 = 0.77), Figure 6A, indicates that the Otsu threshold explains approximately 80% of the Z variance in overall. As consequence, THLD and MRE are strongly related (R2 = 0.70) as well as the MRE and Z (R2 = 0.74), Figure 6B and C, respectively. Also,~~ we observed ~~a pattern between the MRE and the tide:~~that the MRE increases at high and low tide for all estuaries, and the lowest errors occur ~~during mid-tide. The difference between~~at mid tide. We found a linear correlation between the mean relative error (MRE), the waterline height (Z), and the Otsu adaptive threshold (THLD), which also demonstrates the aforementioned tide-level dependency. For instance, we found that the THLD and the MRE are correlated by R2 = 0.58 (Figure 7b); The THLD and the Z by R2 = 0.82 (Figure 7a), and MRE and Z by R2 = 0.68 (Figure 7c). However, whether a water is collected on the flooding ~~and~~or the ebbing ~~tides~~tide cycles do not ~~seem to interfere in the waterline-derived SDB accuracy; we hypothesised that water draining off the intertidal during ebbing tides might cause inaccuracies in waterline detection. The linear trend of the relationship between MRE, Z, tidal level and the Otsu threshold across different estuaries reflects the similarities of these sites in terms of environmental characteristics such as intertidal zone sediment colour, water turbidity/colour, spring tidal range and the coverage of the intertidal area relative to the overall area of the estuary. In Sect. 3.3, we use the relationship between THLD and MRE to~~ affect the waterline-SDT accuracy. Equation 8 (Figure 6c) is then applied to remove the statistical bias in the waterline-~~derived SDB~~SDT for Tauranga Harbour, ~~what~~which we ~~hereafter called "~~refer to as the statistical correction~~".~~ (Sect. 2.4.1).

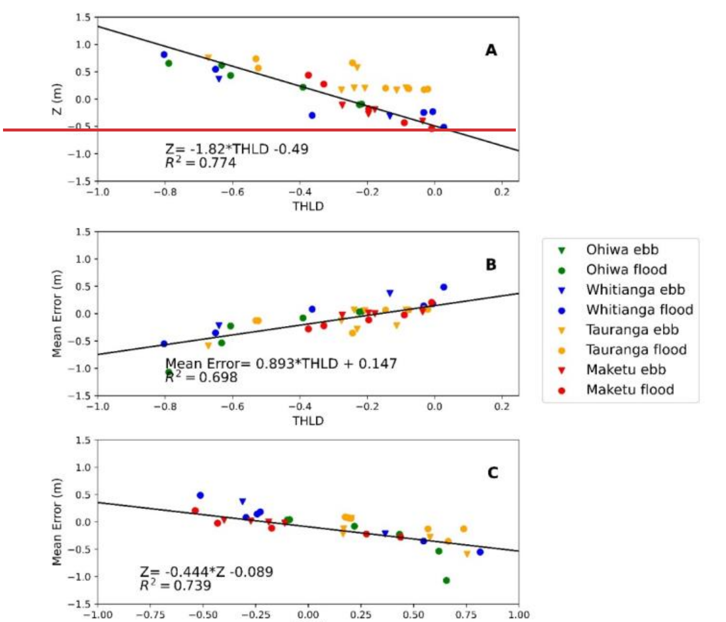

$$\mathrm{MRE} = -0.492 * \mathrm{Z} - 0.089 \quad (8)$$

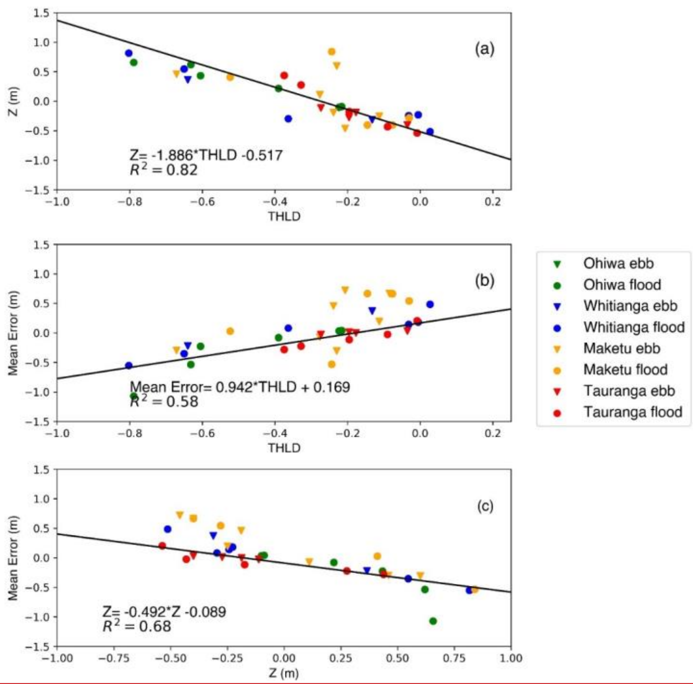

Figure 7: Statistical relationships at all estuaries (Ōhiwa, Whitianga, Tauranga, Maketū): ~~[A]~~(a) water level Otsu threshold (THLD) and observed water level (Z); ~~[B]~~(b) THLD and the SDB mean relative error per image; ~~[C]~~(c) Z and the SDB mean relative error per image R2.

~~**3.2 Comparison between the Waterline and Stumpf-ratio methods for intertidal zones**~~

~~The distribution of the relative vertical error (RE) of Tauranga Harbour's waterline-derived SDB (primary SDB) and Stumpf-derived SDB for intertidal zones are showed in Figure 7. In the waterline-derived SDB (Figure 7 A1, B1, C1, and D1), gaps between the waterlines occur because of the limited number of images used to cover the entire tidal range; although Sentinel-2 acquires images every 5 days, they are often not useable due to cloud cover. The SDB is generally shallower or further seaward than the LiDAR — as the negative RE indicates (see Sect. 2.3) — with the worst estimates in the tidal flat's upper region (bluer colour dots). The positive RE values are concentrated in the estuary's wide flat region (Figure 7 B1), which has a complex bathymetry. In addition, the extensive banks of seagrass located in this area may also contribute to poor waterline extraction (Figure 7 A and B), because seagrass changes pixel reflectance around the waterline.~~

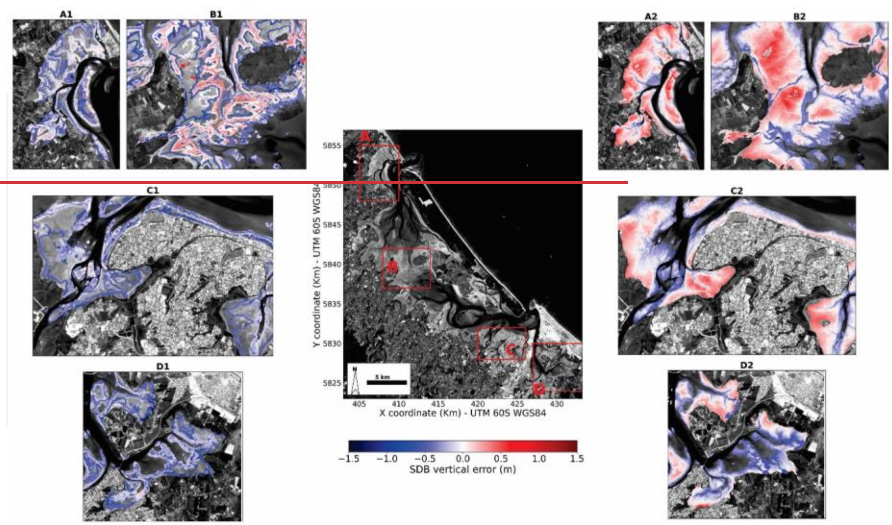

~~Figure 7: Estimated SDB and corresponding relative vertical error for intertidal zone in Tauranga Harbour using~~ 3.3 The statistical and dynamical corrections

The waterline-~~derived (A1, B1, C1,~~SDT (Sect. 2.2), the statistically (Sect. 2.4.1 and ~~D1)~~3.1), and ~~stumpf-ratio (A2, B2, C2, and D2) techniques. Background image: ESA Sentinel 2A.~~

~~The Stumpf-derived SDB (Figure 7: A2, B2, C2, D2) allows the water depth to be assessed on a pixel by pixel basis, with a resolution of 10 m in~~ the ~~case of Sentinel Copernicus data; however the associated error (RMSE=25 cm) is higher than the~~dynamically (Sect. 2.4.2) corrected waterline-~~derived SDB (RMSE=~~SDT showed an overall RMSE equal to 20~~cm). In the Stumpf-derived SDB, the intertidal zone becomes flatter; the positive and negative errors are located in the upper and lower parts of the tidal flats~~, 18 and 19 cm, respectively~~, while in the middle regions a better approximation is estimated (whiter colour dots). Because of the shallow water column in the intertidal zones, the relationship between the log-ratio and depth cannot be properly assessed because of the insufficient variability in the data used to define the log-ratio/depth relationship, which leads to a low coefficient of determination (R2=0.09) between the green/blue band ratio and the LiDAR depth in the intertidal zone during the calibration of Stumpf-ratio technique. This assumption is confirmed by the higher correlation coefficient (R2=0.31) obtained when the same method is applied to the deepest parts of the estuary.~~

~~3.3~~ (Figure 8). The statistical ~~and dynamical corrections~~

~~The uncorrected waterline-derived SDB, the statistically (see Sect. 3.1) and the dynamically corrected waterline-derived SDB results for each image are shown in Figure 8. The overall RMSE is equal to 20, 18 and 19 cm for the uncorrected SDB, statistical and dynamical corrections, respectively. For the uncorrected SDB, the strong relationship between tide level and error in the SDB is once more presented. For instance, in the images acquired during the high and mid-tide (Figure 8, images 6–9) are associated with the highest error values, while smaller errors occur during low-tide (Figure 8, images 1–5).~~

~~The statistical~~ correction is effective where the ~~primary SDB presents strong bias~~SDT is strongly biased (e.g.~~,~~., Figure 8, images 4 and 9). However, for the cases where the uncorrected ~~SDB is a~~SDT shows good ~~approximation~~results (Figure 8, images 1–3), the statistical correction worsens the bathymetric estimates~~,~~ by increasing the corresponding bias. The dynamical correction is more effective ~~in the cases where~~when the waterline is extracted from images collected at mid to high~~ tides~~ tides Figure 8; images 4–9) than at low tides (Figure 8; images ~~4–9~~1–3), improving the RMSE values by 5 cm on average. However, ~~during low tides (Figure 8, images 1–3),~~ the estimates can worsen during low tides by 10.5 cm on average.

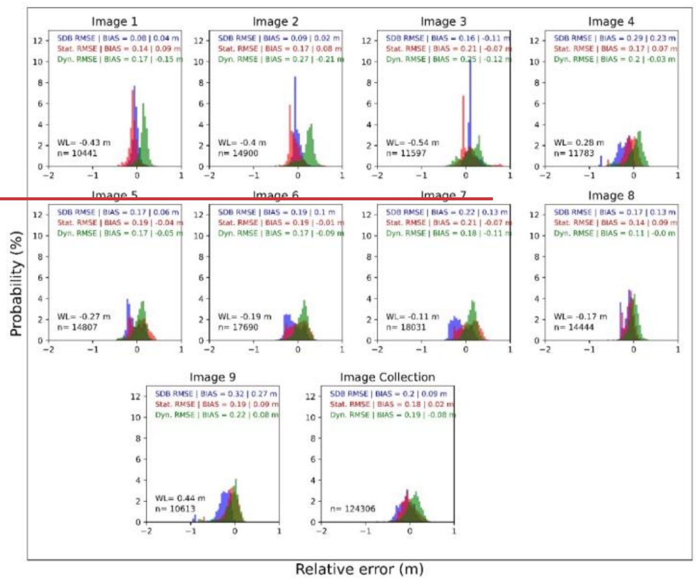
Image 1
SDB RMSE | BIAS = 0.08 | 0.04 m
Stat. RMSE | BIAS = 0.14 | 0.09 m
Dyn. RMSE | BIAS = 0.17 | -0.15 m
WL= -0.43 m
n= 10441
Image 2
SDB RMSE | BIAS = 0.09 | 0.02 m
Stat. RMSE | BIAS = 0.17 | 0.08 m
Dyn. RMSE | BIAS = 0.27 | -0.21 m
WL= -0.4 m
n= 14900
Image 3
SDB RMSE | BIAS = 0.16 | -0.11 m
Stat. RMSE | BIAS = 0.21 | -0.07 m
Dyn. RMSE | BIAS = 0.25 | -0.12 m
WL= -0.54 m
n= 11597
Image 4
SDB RMSE | BIAS = 0.29 | 0.23 m
Stat. RMSE | BIAS = 0.17 | 0.07 m
Dyn. RMSE | BIAS = 0.2 | -0.03 m
WL= 0.28 m
n= 11783
Image 5
SDB RMSE | BIAS = 0.17 | 0.06 m
Stat. RMSE | BIAS = 0.19 | -0.04 m
Dyn. RMSE | BIAS = 0.17 | -0.05 m
WL= -0.27 m
n= 14807
Image 6
SDB RMSE | BIAS = 0.19 | 0.1 m
Stat. RMSE | BIAS = 0.19 | -0.01 m
Dyn. RMSE | BIAS = 0.17 | -0.09 m
WL= -0.19 m
n= 17690
Image 7
SDB RMSE | BIAS = 0.22 | 0.13 m
Stat. RMSE | BIAS = 0.21 | -0.07 m
Dyn. RMSE | BIAS = 0.18 | -0.11 m
WL= -0.11 m
n= 18031
Image 8
SDB RMSE | BIAS = 0.17 | 0.13 m
Stat. RMSE | BIAS = 0.14 | 0.09 m
Dyn. RMSE | BIAS = 0.11 | -0.0 m
WL= -0.17 m
n= 14444
Image 9
SDB RMSE | BIAS = 0.32 | 0.27 m
Stat. RMSE | BIAS = 0.19 | 0.09 m
Dyn. RMSE | BIAS = 0.22 | 0.08 m
WL= 0.44 m
n= 10613
Image Collection
SDB RMSE | BIAS = 0.2 | 0.09 m
Stat. RMSE | BIAS = 0.18 | 0.02 m
Dyn. RMSE | BIAS = 0.19 | -0.08 m
n= 124306
Probability (%)
Relative error (m)

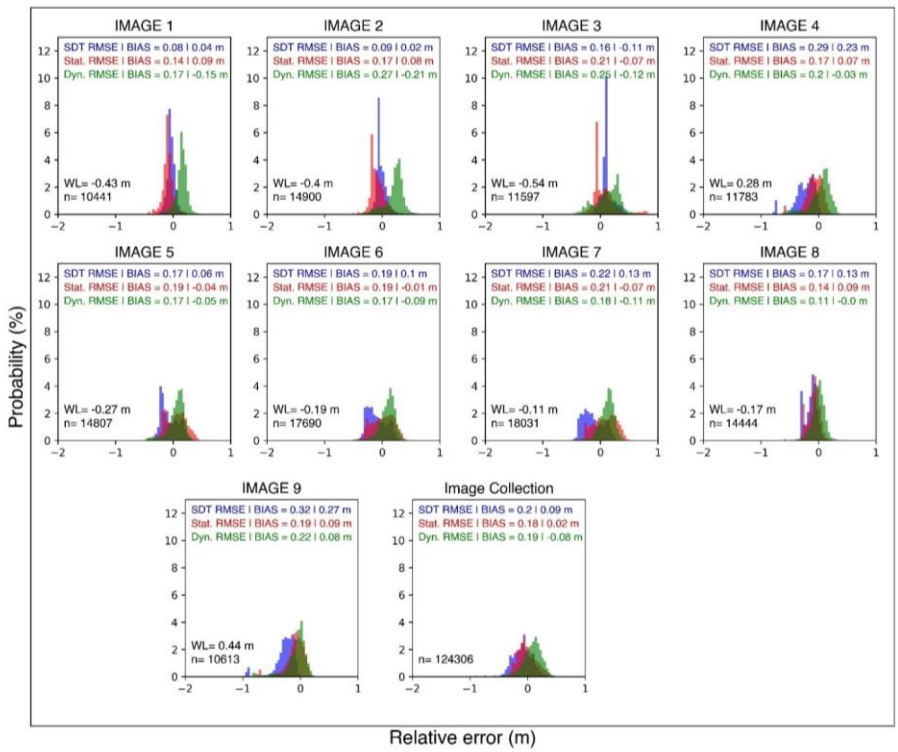

Figure 8: Histograms of the waterline-derived ~~SDB~~SDT relative error (RE) for each image in the collection for Tauranga Harbour: ~~uncorrected SDB~~waterline-SDT (blue), ~~statistical correction~~statistically corrected waterline-SDT (red) and ~~dynamical correction~~dynamically corrected waterline-SDT (green). RMSE, BIAS, ~~observed water level~~waterline height (WL), and number of waterline samples (n) are shown.

~~The limited improvement of the proposed corrections — 2 and 1 cm in terms of RMSE, for statistical and dynamical corrections, respectively — can be due the limitations in the LiDAR data (survey performed in the year 2015, with +-20 cm vertical error), and hydrodynamic model predictions (average RMSE= 8cm and MAE = 20 cm), limiting the potential improvements that could be made to the method's accuracy.~~

~~In numerical models, although the waterline position is expected to be highly sensitive to the spatial grid resolution and interpolated bathymetry smoothness, the model is expected to obtain accurate water level predictions if properly calibrated and validated. To better illustrate the dynamical correction, we show the waterline position along three different profiles from Tauranga Harbour in Figure 9. The uncorrected SDB is represented for these three different waterline positions (coloured~~

~~circles: red, green, blue) with their corresponding heights (solid line) given from the observed water levels in the Ōmokoroa tide gauge at the time when the satellite acquires the image. The corresponding waterline position is also plotted with the height provided from the hydrodynamic model (triangles and dashed lines). The difference made by using the hydrodynamic model to assess the waterline height can vary spatially throughout the Harbour. For instance, while in P1 the dynamical correction generally causes the height to be lower than the LiDAR height, whereas in P2, the SDB more closely represents the level measured by the LiDAR. In P3, the red and blue lines improve, whereas the green line worsens.~~

~~Some limitations in the waterline method can also be assessed by analysing the profiles in Figure 9. For instance, in P2 and P3, the red and green observed waterlines are close to each other even though the tidal records show that the vertical difference should be almost 20 cm. However, when they are compared with the water level associated with the hydrodynamic model, they are roughly at the same elevation. The morphology in the intertidal area also plays a role. In P3, the terrain is quite steeply sloped, and in P2, the morphology undulates up and down which could cause some inaccuracies given that the resolution of the Sentinel-2 images is 10m. Additionally, it is important to note that regardless of whether there is a bimodal or unimodal distribution of the NDWI within in the intertidal zone, the Otsu threshold is defined by detecting the value that maximizes the within-class variance between two classes of a distribution. This means that even when all intertidal image pixels are flooded or dry, a threshold will be set and pixels will be selected as being the waterline, e.g. the peaks of high and low tide.~~

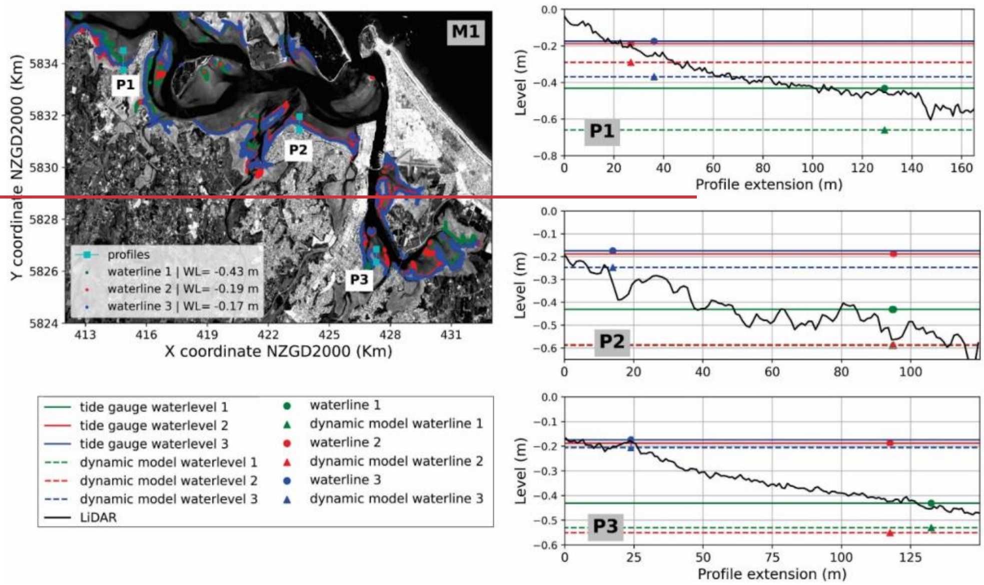

~~**Figure 9: Profile analysis of the dynamical correction. [M1] Three waterline positions (blue, red, green) extracted from 3 different images corresponding to the observed water levels (WL) at Ōmokoroa. [P1, P2, P3] The position (dots) and WL (continuous lines) of the detected waterline and their corresponding dynamically corrected WL (dashed lines) and waterline position (triangles). The continuous black line is the LiDAR data along each profile. Background image: ESA Sentinel 2A.**~~

3.4 Prediction of water level using the SDB

The simulation scenarios showed that ~~it is possible to~~the combined use of SDB and SDT can obtain similar~~,~~ or ~~even enhanced~~better water level predictions~~, by~~ compared to those predicted using ~~the SDB rather than the~~only surveyed bathymetry~~, Figure 10. The~~ (although the log-ratio method requires some in situ calibration data). Figure 10 illustrates the average error parameters ~~evaluated for observations from the~~ calculated when comparing the model output with the record of the three tide gauges ~~(Ōmokoroa, Hairini and Oruamatua) show that, despite the lower density of estimated points, the use of waterline-derived SDB (S2) has a superior performance (RMSE=7.4 cm, MAE=24.3 cm, R2=0.97) to the Stumpf-derived SDB-S3 (RMSE=9.7 cm, MAE=29 cm, R2=0.96). The S4 scenario shows that by combining different SDB sources — waterline method~~. For a detailed assessment of each one of the gauges, please consult Supplement D. In S4, the waterline-SDT for intertidal zones ~~and Stumpf-~~combined with the ratio ~~method~~-log-SDB for ~~deeper areas of the estuary — it is possible to~~shallow waters can predict the astronomical tide ~~with similar accuracy to using survey~~more accurately (RMSE~7cm; MAXE~25cm). In the S1 results, the model uses surveyed bathymetry (S1~~).~~) with poorer performance (RMSE~9cm; MAXE~32cm). Specifically, at the location of the ~~Oruamatua~~Ōruamatua tide gauge, the predictions were ~~strongly enhanced~~improved in the

Formatted: Keep with next

S4 scenario (RMSE=5cm; ~~MAE~~MAXE=17cm) ~~in comparison~~compared to S1 (RMSE=13cm; ~~MAE~~MAXE=42cm), ~~which can be seen in~~see Figure ~~S8~~S9, Supplement D.

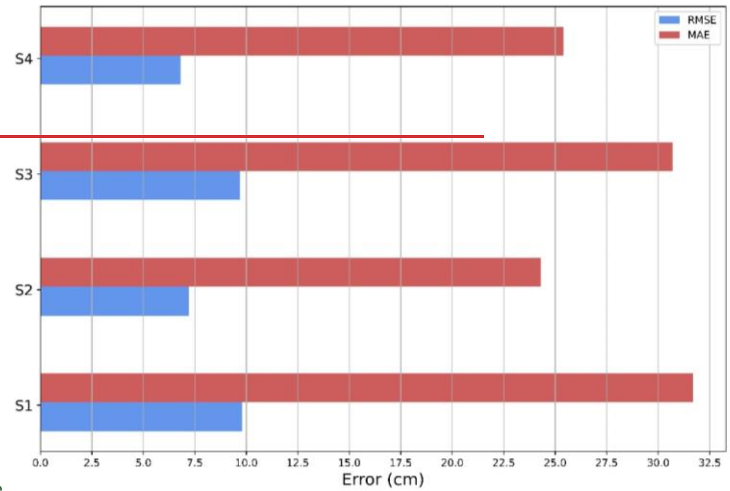

Regarding the

605 scenarios where SDTs replace just the intertidal topography, S2 (waterline-SDT) provided superior performance (RMSE=7.4 cm, MAXE=24.3 cm, R2=0.97). In S3, the model uses ratio-log-SDT and shows poorer performance (RMSE=9.7 cm, MAXE=29 cm, R2=0.96).

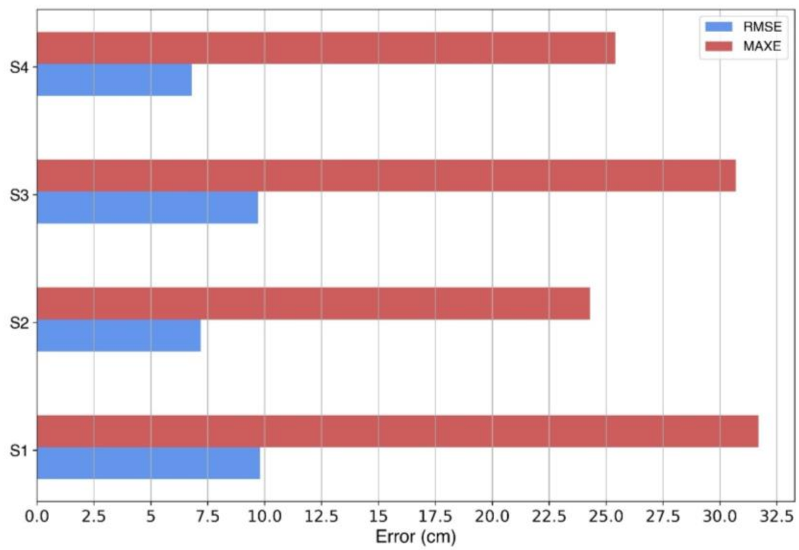

Figure 9: The average parameter errors ~~of the four~~calculated considering the results at the 3 tide gauge locations (Ōmokoroa, Hairini, Ōruamatua) for each simulation scenarios (S1, S2, S3, and S4) — RMSE (blue bar), ~~MAE~~MAXE (red bar~~) — for evaluated at the 3 tide gauge locations (Ōmokoroa, Hairini, Oruamatua~~).

~~The estuary's inner channels are where the major differences in the water level predictions occur, which reflects the numerical grid spatial resolution (20m) limitations in representing the flooding and drying within grid cells around narrow channels, as illustrated for the scenarios S1 and S4 in Figure 11, referring to the differences in the maximum (panel A) and minimum (panel B) water level in each grid cell over the entire simulation. The occurrence of additional dry cells (e.g. in the harbour's northern and central region) is apparent in S4 when compared to S1 for highest (panel A) and lowest (panel B) water levels. This is caused by the reflectance of areas covered by seagrass, that which interfere with the ability to detect the waterline/seabed using remote sensing.~~

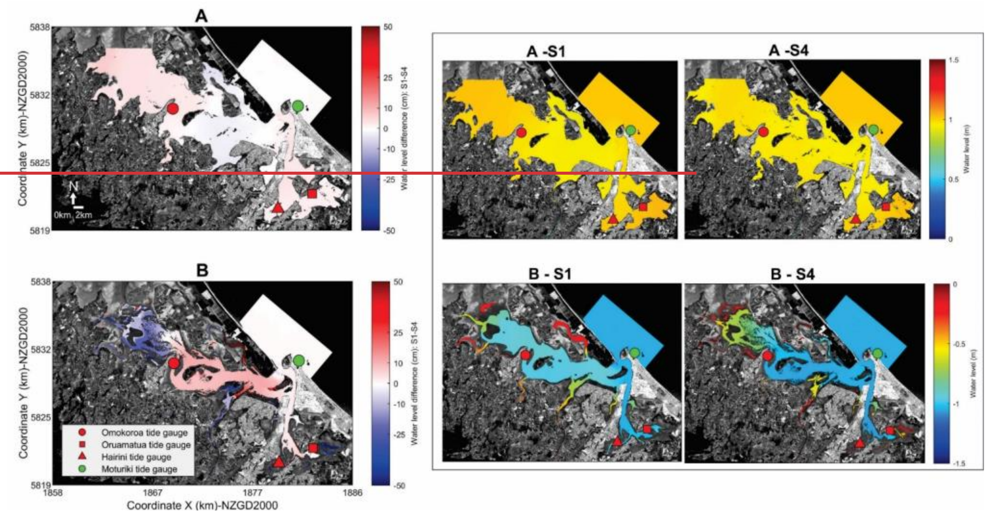

The good agreement between scenarios S1 and S4 in Ōmokoroa, Hairini, and Ōruamatua can also be extended to the entire model domain. For instance, the difference between S1 and S4 is close to zero at the maximum water level in each grid cell over the entire simulation (Figure 10, panel a). However, major differences in the water level predictions occur in the estuary's inner channels at the minimum (low-tide) water level at each grid cell (Figure 10, panel b).

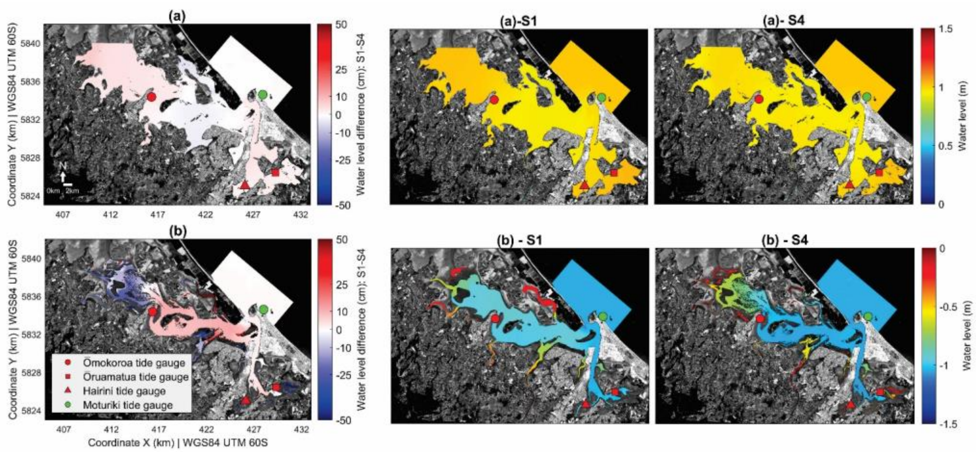

Figure 10: Spatial difference between the hydrodynamic model output using survey bathymetry (S1) and the waterline-derived plus ~~Stumpf~~ ratio-log derived SDB (S4). High (~~A~~a) and low tide condition (~~B~~b), where positive means that the water level S1 is higher than S4. Background image: ESA Sentinel 2A. Date and time of the image acquisition: 18/12/2018 10:15 h.

4. Discussion

We proposed a semi-automated framework to derive bathymetry and topography from satellite images by applying two well-known methods: the waterline method for elevation data in intertidal zones (e.g., Khan et al., 2019; Fitton et al., 2021; Jia et al., 2021) and the ratio-log empirical method for shallow waters (Stumpf et al. 2003). We combined the satellite-derived elevation techniques with cloud computation and database, allowing us to rapidly estimate topographic and bathymetric data for several locations simultaneously on a regional and large-scale (also shown in Jia et al., 2021; Fitton et al., 2021; Traganos et al., 2018). Here we focused on using these combined technologies for the hydrodynamic modelling of extreme water levels (caused by surges and tides) in enclosed estuaries. Our work adds to growing body of work on applying satellite techniques as an alternative to monitoring the coastline (Turner et al., 2021).

Our discussion is presented in four parts. In the three first parts, we addressed our first and second specific objectives, discussing our main findings and limitations when applying the waterline and ratio-log methods, including suggestion for improvements. In the fourth part, we addressed our third objective, discussing the challenges of using SDTs and SDBs in modelling extreme water levels within a complex-morphology estuary.

4.1 Our proposed waterline method for deriving topography from space-borne images and its limitations.

The waterline method compares well to LiDAR data in our study sites — considering that the topography in the intertidal zone ranges between -1.12 m to +2.98 m relative to MSL (see Table 3), and the vertical and horizontal accuracy of the LiDAR data are 20 cm and 60 cm, respectively. Although it is hard to directly compare different studies because they are conducted in different coastal areas, our results show a similar bias to other studies performed in similar estuarine environments. For instance, Salameh et al. (2020), applied the waterline method to Arcachon Bay in France, with the estimated DEM accuracy of RMSE = 0.27 m; Bué et al. (2020) generated SDTs for Azinheira estuary (Portugal) based on logistic regression with an RMSE = 0.6 m.

Despite the good results of waterline-SDT in NZ estuaries, the method is sensitive to the correct positioning and height-assigning of the waterline. Our results also shows that environmental conditions such as the complex morphology, varied bed substrates, and groundwater seepage could reduce the accuracy of the waterline position. Also, the location of the tide gauge used to assign the waterline height is important. For instance, Maketū estuary is a small estuary with complex morphology, and the tide gauge of Moturiki is located at approximately 27 km from the estuarine entrance, which likely explains the very low accuracy of SDT for that location. Furthermore, using just one tide gauge to assign the waterline height can add vertical error to the estimates because it does not account for the tide deformation and propagation in such a complex environment. Maketū is also undergoing staged engineering works to remove former flood protection which could have caused changes to the bathymetry between images and after the LiDAR survey was undertaken.

Complex morphology affects the estimates differently over different parts of the topographic profile — waterlines closer to the MSL (water level ~0 m) are more accurate, and waterlines closer to the peak of the high and low tides are less accurate (see Sect. 3.3). Our results corroborate those of Liu et al. (2013), who quantitatively analysed the waterline method in Dongsha Sandbank, China (an exposed coastal area). In their study, the authors have found that the main error source in the waterline method is linearly correlated to the slope and area of the intertidal zone. Furthermore, having enough images to characterise the morphology of the study site is also a limiting factor in the waterline method, as pointed out by several studies (Salameh et al., 2019; Liu et al., 2013). Our results are also clearly affected by the number of images in our collection. For instance, we observed gaps between different waterlines, where no topographic data could be derived, shown in Fig. 7 (Sect. 3.2). Although we have used Sentinel-2 images acquired every five days, they are often not useable due to cloud coverage.

The bed substrate can directly affect the waterline positioning, especially in New Zealand estuaries, where clear water is common. For instance, in Tauranga Harbour the seagrass banks, (Ha et al., 2020) and the groundwater seepage (shown to cause an error in water line detection in Huisman et al., 2011) can abruptly change the reflectance of the pixels around the waterline, especially in the centre part of the estuary, where the seagrass banks can be seen (Figure S3). We used the adaptive

Otsu method (Nobuyuki Otsu, 1979) to detect the edges between water and intertidal zones. The method showed good performance for determining the waterline location in estuaries, corroborating studies on lakes, rivers, water reservoirs (Donchyts et al., 2016), and coastlines (Vos et al., 2019). We have also tested the edge identification by calculating the mean or the median of NDWI distribution following approaches in previous studies (Sagar et al., 2017; Bishop-Taylor et al., 2019), but these did not performance as well (not shown). However, the Otsu method defines a threshold by detecting the value that maximises the within-class variance between two classes of a grey-scale distribution, which can cause two limitations: first, the inability to correctly detect waterlines in images with complex conditions, i.e., where the water is clear, and the bed substrates reflectance can be seen in the satellite images; second, the Otsu threshold method will detect waterlines even when all intertidal pixels are flooded or exposed, adding bias in the extremes of the topographical profiles (peak of high or low tide).

There are currently several methods for edge detection that have been implemented in waterline-SDT that can potentially overcome the issues highlighted above. One practical solution would be the manual identification of the waterline; however, it is subjective and labour-intensive when applied over a large area and in multiple study sites. Another way would be to apply image segmentation techniques, for instance, K-means clustering techniques applied to edge detection (Salameh et al., 2020). Alternatively, the simple identification of sea-grass banks could be used to remove areas where the waterline is poorly detected prior to analysis. Ha et al. (2020) identified seagrass using ensemble-based machine learning algorithms. Caballero and Stumpf (2020) identified algae and seagrass by using an empirical formula to calculate the maximum chlorophyll index, which uses three different optical bands to explain the radiance peak at the red-edge band.

4.2 Our proposed correction methods for waterline-SDTs.

Our proposed correction methods (i.e., statistical and dynamical) for the SDT only resulted in a 1–2 cm improvement across the case-study estuary. However, our insights into why and where the correction resulted in improvements provide the basis for further work (e.g., when more imagery becomes available to test error sources more thoroughly). The statistical relationship between the error and the waterline height, the elevation on the tidal flat (LiDAR) and the waterline detection threshold in all four studied estuaries allowed us to set a semi-independent framework to correct the vertical level in the waterline derived SDT. For instance, we can first learn the relation between THLD and MRE in similar estuaries. And then apply the correction to an entirely different study area with similar intertidal zone properties. For instance, estuaries with similar sediment colour, water turbidity, spring tidal range and intertidal area coverage.

The dynamical correction gives more realistic waterline heights because it accounts for the tide propagation within the estuary. However, the approach did not significantly improve the SDT. We hypothesized three reasons for the limited improvement. First, inaccuracies in horizontal waterline position may be more important that inaccuracies in the waterline height. When correcting the waterline height (vertical errors), we are not eliminating the horizontal errors. Figure 11 shows three different waterline positions along three different profiles. The uncorrected waterline-SDT is represented for three different waterline positions (coloured circles: red, green, blue) with their corresponding heights (solid line). The corresponding dynamically corrected waterline position and height are plotted, represented by the triangles and dashed lines, respectively. In Figure 11, we observed that some of the dynamically corrected waterlines (i.e., coloured triangles) are further seaward or landward in the topographic profile from where they should be. For instance, all the corrected waterlines in P1 (i.e., red, green and blue triangles) should be further seaward than they are. In P2, the blue-triangle waterline should be slightly landwards, and the red- and green-triangle waterlines, further seaward. In P3, all corrected waterlines should be further seaward. However, when the waterline is well positioned, waterline heights can be closely corrected to the LiDAR data; for instance, in P2 for all waterlines (dashed lines); and in P3 for the red and blue dashed lines.

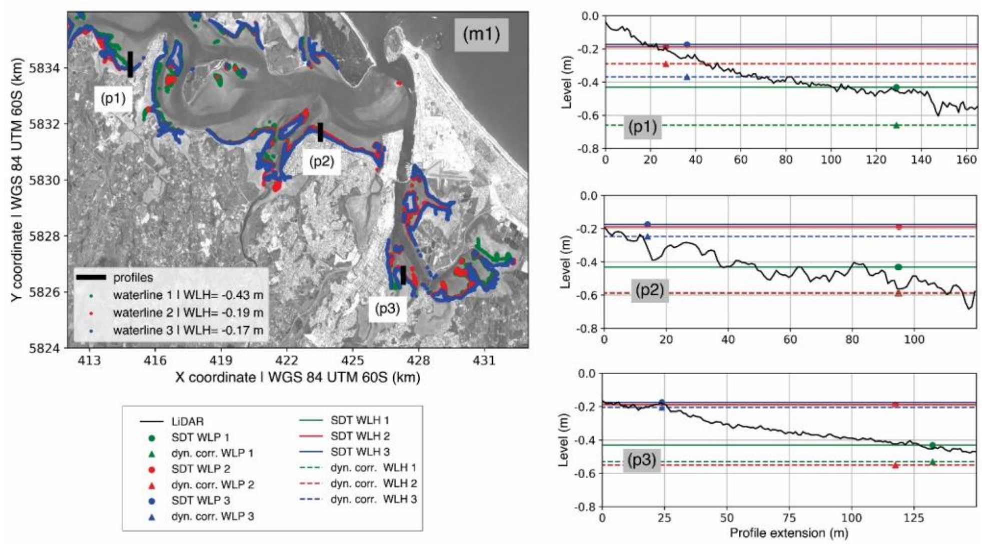

Figure 11: Profile analysis of the dynamical correction in three different profiles (p1, p2, p3). [m1] shows the location of the profiles in Tauranga Harbour. [p1, p2, p3] shows the waterline height (WLH) and position (WLP) of three different waterlines (green (1), red (2), blue (3)) derived from the waterline-STD (STD) and their corresponding dynamically corrected (dyn. corr.) WLH and WLP. The continuous black line is the LiDAR data along each profile. Background image: ESA Sentinel 2A.~~4.1 Insights about the waterline-method for satellite derived bathymetry~~

~~In our study, we used a waterline method to derive bathymetry from satellite images which has been trialled in other studies (Khan et al., 2019; Mason and Davenport, 1996; Ryu et al., 2002). Although our proposed correction methods (i.e. statistical and dynamical) for the SDB only resulted in 1–2 cm improvement across the estuary, our insights into why and where the correction resulted in improvements provide the basis for further work (e.g.~~ Date and time of the background image acquisition: 18/12/2018 10:15 h.

The second factor that can influence the correction's performance is the hydrodynamic model accuracy — especially at low tide, as can be seen in Figure 10. The spatial resolution of the numerical grid (20 m) can limit the model's ability to correctly solve the flooding and drying within grid cells around narrow channels, potentially adding horizontal bias to the waterline heights. Moreover, the third limiting factor is the LiDAR data horizontal and vertical accuracy, which limits the potential correction. The use of hydrodynamic modelling to assign the waterline heights is a common practice when generating SDTs (e.g., Liu et al., 2013; Khan et al., 2019; Salameh et al., 2020; Fitton et al., 2021). However, in most of the cases, the studies cover an extensive area, with exposed coastlines or sand banks, in which regional tide models are used where there are not enough tide gauges to provide tide levels (Liu et al., 2013; Khan et al., 2019; Fitton et al., 2021). In just a few of these studies, enclosed estuaries were studied by setting up local-scale hydrodynamic modelling (e.g., Salameh et al., 2020; Liu et al., 2013).

For instance, in Arcachon bay (France), Salameh et al. (2020) compared the waterline-SDTs that were generated by assigning waterline heights according to single-location tide gauges, single-location model point output and grid hydrodynamic model output. Similar to our results, they found that the waterline heights assigned by using grid model output did not improve the SDTs compared with using a single-location tide gauge within the estuary. They explained unexpected result as due to the slope of the tidal flat, and the model's inability to provide accurate sea level heights over the intertidal area. Similarly, Liu et al. (2013) used a regional tide model for the South Yellow Sea (China) to assign waterline heights to a local-scale study in Dongsha Sandbank (an exposed tidal flat), which limited the vertical accuracy of the SDT up to 30 cm (corresponding to the model's accuracy).

4.3 Comparison between the waterline-method and ratio-log for intertidal zones.

Our results show that the waterline is a better method than the ratio-log for deriving topography using satellite images. The distribution of the relative vertical error (RE) of Tauranga Harbour's waterline-SDT and ratio-log-SDT for intertidal zones are shown in Figure 12. In the waterline-SDT (Figure 12 a1, b1, c1, and d1), the SDTs are ~~when more imagery becomes available to test error sources more thoroughly).~~ ~~The statistical relationship between the error and the observed local water level, the elevation on the tidal flat and the waterline detection threshold in all 4 studied estuaries allowed us to set a semi-independent framework to correct the vertical level in the waterline-derived SDB. For instance, we can learn the relation between THLD and MRE in similar estuaries, and then apply the correction to an entirely different study area that has similar environmental properties (e.g. intertidal zone sediment colour, water turbidity/colour, spring tidal range and the coverage of the intertidal area relative to the overall area of the estuary). At this stage, the dynamical correction did not significantly improve the SDB because of the limitations in model performance and LiDAR data; however, similar approaches have been tested and validated~~

Formatted: Keep with next

~~for open estuarine areas proving that the effects of tidal propagation can be corrected (Bishop-Taylor et al., 2019; Khan et al., 2019; Mason et al., 1997).~~

~~Regarding the error source in the waterline method, our findings are similar to previous studies in that errors originated from the estuary's complex morphology, tidal range covered by the satellite images, and the ratio between water level and flooding/drying area in the tidal flat (Bué et al., 2020; Liu et al., 2013; Mason et al., 2001). In addition, the environmental conditions and unexpected variations in the image reflectance caused by seagrass banks (Ha et al., 2020) and/or groundwater seepage (Huisman et al., 2011), could also affect the SDB accuracy, likely contributing to our waterline-SDB being shallower than the LiDAR over the lower intertidal.~~

~~In comparison to other SDB techniques, our method showed a better or similar performance. For instance, the waterline method is an improvement on the Stumpf-ratio method (Caballero and Stumpf, 2019; Stumpf et al., 2003), despite the higher density of estimated water depth points (pixel-by-pixel resolution) that this log-ratio method offers. In addition, our method does not depend on calibration with surveyed bathymetry in order to establish a vertical reference (Jupp, 1989; Lyzenga, 1985; Stumpf et al., 2003). However, more accurate bathymetric derivations could be generated if physical based algorithms such SOA (Lee et al., 2011; Wei et al., 2020) or water turbidity correction methods (Caballero and Stumpf, 2020) were applied. In comparison to previous work using the SAR waterline techniques in larger and open estuaries and coastal areas (Bell et al., 2016; Catalao and Nico, 2017; Mason and Davenport, 1996), similar methods using waterline method and optical images (Bishop-Taylor et al., 2019; Khan et al., 2019; Sagar et al., 2017), and logistic regression approach (Bué et al., 2020), our approach can lead to average errors in the same order of magnitude (14 to 40 cm).~~

~~The use of an adaptive waterline threshold based on the Otsu method (Nobuyuki Otsu, 1979) showed good performance for determining the waterline location in estuaries, corroborating results of similar studies on lakes, rivers, water reservoirs (Donchyts et al., 2016), and coastlines (Vos et al., 2019). For our study site, this approach performed better if compared to the thresholds determined by the mean, or the median of NDWI distribution as used in previous studies (Bishop-Taylor et al., 2019; Sagar et al., 2017)~~

~~4.2 Hydrodynamic modelling assessment~~

~~Bathymetric data are fundamental for solving the hydrodynamic equations in shallow water; hydrodynamic models and flooding risk assessments in coasts and estuaries are therefore highly sensitive to depth values (Cea and French, 2012; Parodi et al., 2020; Pedrozo-Acuña et al., 2012). Our results show that inaccuracies occur especially in inner channels and seagrass banks, which means that the prediction of local short-term water level responses could be significantly affected. However, during the high tide, the resulting water level from SDB and survey scenarios are in good agreement in the majority of the simulated estuary domain and at the location of the tide gauges. Additionally, the overall shape of the bathymetry together with the length of estuary are the factors that affect the tidal response to sea-level rise in these environments (Du et al., 2018), which lead us to conclude that minor/ local irregularities in the bathymetry estimates do not substantially affect long term predictions for coastal management application.~~

~~Although the differences in the resulting water level between the SDB and in-situ bathymetry simulation scenarios compare well, our simulations were only conducted in one estuary (albeit a large and relatively complex estuary). Numerical simulations considering other estuaries and the storm surge should be evaluated as well, in order to know whether the errors on the SDB estimation could affect the tide-surge interactions, which is an important process to be considered in water level modelling (Spicer et al., 2019; Wankang et al., 2019; Zheng et al., 2020).~~

generally shallower or further seaward than the LiDAR — as the negative RE indicates (see Sect. 2.3) — with the worst estimates in the tidal flat's upper region (bluer colour dots). The positive RE values (redder colour dots) are concentrated in the estuary's wide flat centre region (Figure 12 b1) and indicate that the estimates are deeper or further landward than the LiDAR data.

The ratio-log-SDT (Figure 12: a2, b2, c2, d2) allows the water depth to be assessed on a pixel-by-pixel basis, with a resolution of 10 m in the case of Sentinel Copernicus data; however, the associated error (RMSE=25 cm) is higher than the waterline-SDT (RMSE=20 cm). In the ratio-log-SDT, the intertidal zone becomes flat; the positive and negative errors are in the upper and lower parts of the tidal flats, respectively. In the middle of the topographic profile, the estimates are more accurate (whiter colour dots). The low data variability (pixels reflectance) probably causes the lower accuracy of the ratio-log-SDT in comparison to the waterline-SDT. The ratio-log (green/blue band ratio) poorly explains the depth (LiDAR data), which leads to a low correlation coefficient (R^2=0.12). This assumption is confirmed by the higher correlation coefficient (R^2=0.24) obtained when the same method is applied to the shallow waters within Tauranga Harbour. In addition, the presence of seagrass in the intertidal zones and shallow water (Figure S3) can potentially worsen the ratio-log-SDT and SDB because it affects the reflectance of the pixel (Geyman and Maloof, 2019; Caballero and Stumpf, 2020).

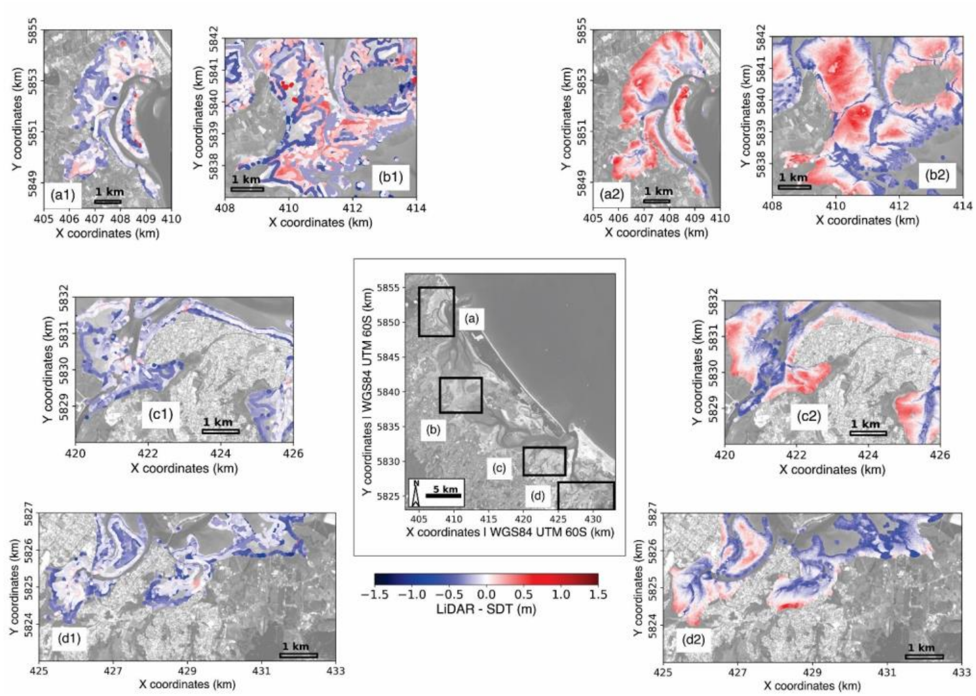

Figure 12: Estimated SDT and corresponding relative vertical error (RE) for intertidal zone in Tauranga Harbour using waterline-derived (a1, b1, c1, and d1 and ratio-log (a2, b2, c2, and d2) methods. Background image: ESA Sentinel 2A. Date and time of the background image acquisition: 18/12/2018 10:15 h.

Numerous estuaries have turbid water, which would reduce the quality of SDBs and SDTs derived from both ratio-log and waterline methods. The ratio-log derivations would be affected by the interference of the suspended material on the light absorption rate through the water column — which could be improved by using methods that adjust the ratio-log method for turbid water (e.g., Caballero and Stumpf, 2020). The waterline derivations would be affected by intertidal zone identification. The NDWI of the pixels in shallow water with a high concentration of suspended materials could have similar values to those in the intertidal zone. Consequently, determining the intertidal areas would be more uncertain.

In addition, image pre- and post-processing are other factors that may improve the accuracy of the SDT and SDB of waterline and ratio-log methods. We used available Sentinel images already pre-processed by using Sen2Cor, which creates surface-reflectance images (see Sect. 2.1). However, several pre-processing tools are available (Pereira-Sandoval et al., 2019). Some of these are designed specifically for use in coastal areas — where water is often turbid, containing a high concentration of suspended sediments and other materials. For instance, the ACOLITE tool (Vanhellemont andRuddick, 2018) has been widely applied in estuaries (e.g., Bué et al., 2020; Salameh et al., 2020; Fitton et al., 2021). In the case of exposed coastal areas or where local wind waves can increase the rugosity of the water surface, filters to eliminate sun glint can be applied (Hedley et al., 2005)

4.4 Hydrodynamic modelling assessment

The bathymetric and topographic data quality is fundamental for reliable hydrodynamic modelling. Despite the limited accuracy of the SDT and SDB (see Sect. 4.1–4.3), our results show that hydrodynamic models using satellite-derived elevation can predict water level with similar accuracy in comparison with models using only surveyed data (see Sect.3.4, Figure 11). Thus, we can infer that the water level modelling may not be sensitive to small uncertainties in the bathymetric data, but rather to the larger scale characteristics of the estuary, such as the width of entrances and overall geometry.

Some of the bathymetric uncertainties can arise from the interpolation technique used to create the DEMs (Circus et al., 2000; Kang et al., 2017, 2020; Salameh et al., 2020) — e.g., spline, kriging, inverse distance weighting (IDW), nearest neighbour, triangulation. However, previous studies have found that uncertainties in the elevation data lead to minor differences in the water level predictions (Cea and French, 2012; Falcão et al., 2013). For instance, Cea and French (2012) showed that water level predictions do not significantly change with vertical uncertainties of up to 1 m in the bathymetry. Similarly, Falcão et al. (2013) have shown that the DEMs created with the same interpolation technique (i.e., kriging) but with a different spatial resolution (i.e., 5 and 50m) did not significantly affect the water level prediction. Corroborating our results, Falcão et al. (2013) also found that the worst predictions are for grid cells where the water level is at a minimum, when comparing these two scenarios. The stream current magnitude and direction predictions are affected the most by the uncertainties in the bathymetric and topographic data (Cea and French, 2012; Falcão et al., 2013). In addition, bed roughness and eddy viscosity are two important calibration parameters highlighted in several studies (Pedrozo-Acuña et al., 2012; Mohammadian et al., 2022; Cea and French, 2012) that we have not explored in this manuscript because of its focus on SDT and SDB, although the parameters were calibrated for the hydrodynamic model.

Despite the uncertainties in the estimates, SDT and SDB can generate a fair approximation of estuary relief, which can be helpful in long-term predictions for coastal management applications. In idealistic numerical studies, the extension and slope of the intertidal zone, the estuary's length, and the width of the mouth are the main factors causing changes in the tidal range within harbours (Khojasteh et al., 2021; Du et al., 2018; Khojasteh et al., 2020). For instance, Du et al. (2018) show that the length of an estuary and intertidal zone slope strongly influences the tidal range. However, the entrance restriction drives the estuarine response to SLR (Khojasteh et al., 2020); the smaller the cross-sectional area of the estuary mouth, the smaller would be the tidal range within the estuary. Moreover, SDT and SDB could be used for data assimilation in numerical modelling, as in Mason et al. (2010), who used the SDT to calibrate a morphodynamic model. Ultimately, the SDTs and SDBs can decrease the uncertainties of flood-risk management in the present and future scenarios of SLR where studies are limited due to lack of elevation data in remote areas such as small islands in developing states (Parodi et al., 2020) and coastal lagoons in developing countries (Pedrozo-Acuña et al., 2012).

Although the differences in the resulting water level between the SDT, SDB, and surveyed bathymetry simulation scenarios show that satellite techniques compare well, our simulations were only conducted in one estuary, albeit a large and relatively complex estuary — where the astronomical spring tides are the main driver for estuarine flooding. Therefore, studies are required in sites with different physical conditions would be useful to validate the use of SDT and SDB more broadly. For instance, estuaries where the storm surge is the main driver for flooding; or/and exposed estuaries where the wave forces can increase the water level (i.e., wave set-up) (e.g., Bertin et al. (2019)). Furthermore, modelling studies focusing on understanding whether or not the use of SDT and SDB properly represent the tide-surge interactions within the estuary are encouraged, due to the importance of the topic in water level modelling (Spicer et al., 2019; Wankang et al., 2019; Zheng et al., 2020), especially in the context of sea level rise.

5. Conclusions

A waterline technique for deriving ~~bathymetry~~topography from multispectral satellite images was developed and its use in hydrodynamic modelling assessed. The simple pre-processing required for the satellite images combined with the use of cloud computing and storage make the present framework highly applicable to regional scale studies. Our main findings show that the accuracy of the waterline ~~SDB~~SDT is similar or even superior to other techniques applied in previous studies~~. The~~ to comparable sites, and similar to the vertical error in the LiDAR dataset used to assess accuracy~~ of the LiDAR measurements and hydrodynamic model limit the efficacy of the statistical~~. Statistical and dynamical corrections~~. Our major findings in the~~ were trailed but provided limited improvements. The hydrodynamic modelling assessment was encouraging, and showed that SDT and SDB techniques have ~~an encouraging~~ potential for use in high water level predictions~~, considering the scenarios~~ (such as associated with higher than normal tides and storm surges). Scenarios using different applications of the SDT and SDB did not show major high tide differences over most of the numerical domain~~. Moreover the~~ for Tauranga Harbour. The use of SDT and SDB for hydrodynamic modelling in estuaries can make flooding assessment for remote coastal areas feasible~~,~~ and ~~provide~~provides a pathway around the need for expensive surveys for economically depressed vulnerable areas.

Code availability

The codes used in this work are available as python notebooks in https://github.com/CostaAndCoasts/Intertidal-zones-satellite-derived-bathymetry.

Credit authorship contribution statement

Wagner L.L. Costa: methodology, data analysis, writing – original draft, visualization. Karin R. Bryan: conceptualization, supervision, writing – review & editing, resources, funding acquisition. Giovanni Coco: Writing – review & editing, supervision.

Acknowledgment

The authors would like to thank Dr. Ben Stewart for numerical modelling assistance. This work was supported by the National Science Challenge: Resilience Challenge "Coasts" programme, GNS-RNC040. Data were supplied by Land Information New Zealand (LINZ), Bay of Plenty Regional Council, and Waikato Regional Council.

References

~~Bell, P. S., Bird, C. O. and Plater, A. J.: A temporal waterline approach to mapping intertidal areas using X-band marine radar, Coast. Eng., 107, 84–101, doi:10.1016/j.coastaleng.2015.09.009, 2016.~~

Almeida, L. P., Efraim de Oliveira, I., Lyra, R., Scaranto Dazzi, R. L., Martins, V. G., andHenrique da Fontoura Klein, A.: Coastal Analyst System from Space Imagery Engine (CASSIE): Shoreline management module, Environ. Model. Softw., 140, 105033, https://doi.org/10.1016/j.envsoft.2021.105033, 2021.

Ashphaq, M., Srivastava, P. K., andMitra, D.: Review of near-shore satellite derived bathymetry : Classification and account of five decades of coastal bathymetry research, J. Ocean Eng. Sci., 6, 340–359, https://doi.org/10.1016/j.joes.2021.02.006, 2021.

Bertin, X., Mendes, D., Martins, K., Fortunato, A. B., andLavaud, L.: The Closure of a Shallow Tidal Inlet Promoted by Infragravity Waves, Geophys. Res. Lett., 46, 6804–6810, https://doi.org/10.1029/2019GL083527, 2019.

Bishop-Taylor, R., Sagar, S., Lymburner, L~~. and Beaman~~., andBeaman, R. J.: Between the tides: Modelling the elevation of Australia's exposed intertidal zone at continental scale, Estuar. Coast. Shelf Sci., 223~~(October 2018),~~, 115–128, https://doi~~:~~.org/10.1016/j.ecss.2019.03.006, 2019.

Bué, I., Catalão, J~~. and Semedo~~., andSemedo, Á.: Intertidal ~~Bathymetry Extraction~~bathymetry extraction with ~~Multispectral Images~~multispectral images: A ~~Logistic Regression Approach~~logistic regression approach, Remote Sens., 12~~(8), 1311, ~~, https://doi~~:~~.org/10.3390/~~rs12081311~~RS12081311, 2020.

Caballero, I. ~~and Stumpf~~andStumpf, R. P.: Retrieval of nearshore bathymetry from Sentinel-2A and 2B satellites in South Florida coastal waters, Estuar. Coast. Shelf Sci., 226~~(June),~~, 106277, https://doi~~:~~.org/10.1016/j.ecss.2019.106277, 2019.

Caballero, I. ~~and Stumpf~~andStumpf, R. P.: Towards routine mapping of shallow bathymetry in environments with variable turbidity: Contribution of sentinel-2A/B satellites mission, Remote Sens., 12~~(3), ~~, https://doi~~:~~.org/10.3390/rs12030451, 2020.

~~Catalao, J. and Nico, G.: Multitemporal Backscattering Logistic Analysis for Intertidal Bathymetry, IEEE Trans. Geosci.~~

Formatted: Widow/Orphan control

~~Remote Sens., 55(2), 1066–1073, doi:10.1109/TGRS.2016.2619067, 2017.~~

Cea, L. ~~and French~~andFrench, J. R.: Bathymetric error estimation for the calibration and validation of estuarine hydrodynamic models, Estuar. Coast. Shelf Sci., 100, 124–132, https://doi~~:~~.org/10.1016/j.ecss.2012.01.004, 2012.

Circus, D., Kingdom, U., Extinction, M., andStrategies, S.: M . D. Hylton 1 and M.B. Hare 1, 6, 455–462, 2000.

Codiga, D. L.: Unified Tidal Analysis and Prediction Using the UTide Matlab Functions, ~~, (September),~~ 59, https://doi~~:~~.org/10.13140/RG.2.1.3761.2008, 2011.

Costa, W., Bryan, K. R., Coco, G., Zealand, N., andZealand, N.: ASSESSING THE USE OF SATELLITE DERIVED BATHYMETRY IN ESTUARINE STORM SURGE MODELS – STUDY CASE : TAURANGA, 2021.

Donchyts, G., Schellekens, J., Winsemius, H., Eisemann, E~~. and van de Giesen~~., andvan deGiesen, N.: A 30 m resolution surfacewater mask including estimation of positional and thematic differences using landsat 8, SRTM and OPenStreetMap: A case study in the Murray-Darling basin, Australia, Remote Sens., 8~~(5),~~ , https://doi~~:~~.org/10.3390/rs8050386, 2016.

Du, J., Shen, J., Zhang, Y. J., Ye, F., Liu, Z., Wang, Z., Wang, Y. P., Yu, X., Sisson, M~~. and Wang~~., andWang, H.~~ ~~V.: Tidal Response to Sea-Level Rise in Different Types of Estuaries: The Importance of Length, Bathymetry, and Geometry, Geophys. Res. Lett., 45~~(1),~~, 227–235, https://doi~~:~~.org/10.1002/2017GL075963, 2018.

Ehses, J. S. ~~and Rooney~~andRooney, J. J.: Depth Derivation Using Multispectral WorldView-2 Satellite Imagery, NOAA Tech. Memo. NMFS-PIFSC-46, ~~(June),~~ 24, https://doi~~:~~.org/10.7289/V5668B40, 2015.

Emanuel, K.: Increasing destructiveness of tropical cyclones over the past 30 years, Nature, 436~~(7051),~~, 686–688, https://doi~~:~~.org/10.1038/nature03906, 2005.

~~Gao, J.: Bathymetric mapping by means of remote sensing: Methods, accuracy and limitations, Prog. Phys. Geogr., 33(1), 103–116, doi:10.1177/0309133309105657, 2009.~~

Falcão, A. P., Mazzolari, A., Gonçalves, A. B., Araújo, M. A. V. C., andTrigo-Teixeira, A.: Influence of elevation modelling on hydrodynamic simulations of a tidally- dominated estuary, J. Hydrol., 497, 152–164, https://doi.org/10.1016/j.jhydrol.2013.05.045, 2013.

Fitton, J. M., Rennie, A. F., Hansom, J. D., andMuir, F. M. E.: Remotely sensed mapping of the intertidal zone: A Sentinel-2 and Google Earth Engine methodology, Remote Sens. Appl. Soc. Environ., 22, 100499, https://doi.org/10.1016/j.rsase.2021.100499, 2021.

Geyman, E. C. andMaloof, A. C.: A Simple Method for Extracting Water Depth From Multispectral Satellite Imagery in Regions of Variable Bottom Type, Earth Sp. Sci., 6, 527–537, https://doi.org/10.1029/2018EA000539, 2019.

Gorelick, N., Hancher, M., Dixon, M., Ilyushchenko, S., Thau, D~~. and Moore~~., andMoore, R.: Google Earth Engine: Planetary-scale geospatial analysis for everyone, Remote Sens. Environ., 202, 18–27, https://doi~~:~~.org/10.1016/j.rse.2017.06.031, 2017.

Ha, N. T., Manley-Harris, M., Pham, T. D~~. and Hawes~~., andHawes, I.: A ~~Comparative Assessment~~comparative assessment of ~~Ensemble-Based Machine Learning and Maximum Likelihood Methods~~ensemble-based machine learning and maximum likelihood methods for ~~Mapping Seagrass Using Sentinel~~mapping seagrass using sentinel-2 ~~Imagery~~imagery in Tauranga Harbor, New Zealand, Remote Sens., 12~~(3), 355,~~ , https://doi~~:~~.org/10.3390/rs12030355, 2020.

Formatted: Widow/Orphan control

Formatted: Widow/Orphan control

Formatted: Widow/Orphan control

Formatted: Widow/Orphan control

~~Huang, W. G., Fu, B., Zhou, C. B., Yang~~Hedley, J. ~~S., Shi~~D., Harborne, A. ~~Q. and Li, D. L.: Shallow~~ R., andMumby, P. J.: Simple and robust removal of sun glint for mapping shallow-water ~~bathymetric surveys by spaceborne synthetic aperture radar~~benthos, Int. ~~Geosci~~J. Remote Sens~~. Symp., 6(C), 2810–2812,~~., 26, 2107–2112, https://doi~~:~~.org/10.~~1109/igarss.2001.978171, 2001~~1080/01431160500034086, 2005.

Huisman, C. E., Bryan, K. R., Coco, G~~. and Ruessink~~., andRuessink, B. G.: The use of video imagery to analyse groundwater and shoreline dynamics on a dissipative beach, Cont. Shelf Res., 31~~(16),~~, 1728–1738, https://doi~~:~~.org/10.1016/J.CSR.2011.07.013, 2011.

Hume, T., Gerbeaux, P., Hart, D., Kettles, H~~. and Neale~~., andNeale, D.: A classification of New Zealand's coastal hydrosystems, ~~, (October),~~ 120, 2016.

IHO, I. H. O.: ORGANISATION HYDROGRAPHIQUE INTERNATIONALE ORGANIZACION HIDROGRAFICA INTERNACIONAL IHO / OHI Publication C-55, 2020.

Jawak, S. D., Vadlamani, S. S~~. and Luis~~., andLuis, A. J.: A Synoptic Review on Deriving Bathymetry Information Using Remote Sensing Technologies: Models, Methods and Comparisons, Adv. Remote Sens., ~~4(2),~~04, 147–162, https://doi~~:~~.org/10.4236/ars.2015.42013, 2015.

~~Jupp~~Jia, M., Wang, Z., Mao, D~~. L. B.: Background~~., Ren, C., Wang, C., andWang, Y.: Rapid, robust, and ~~extensions to depth of penetration (DOP)~~automated mapping of tidal flats in ~~shallow coastal waters, Collect. Conf. Pap. Descr.~~China using time series Sentinel-2 images and Google Earth Engine, Remote Sens. Environ., 255, 112285, https://doi.org/10.1016/j.rse.2021.112285, 2021.

Kang, Y., Ding, X., Xu, F., Zhang, C., andGe, X.: Topographic mapping on large-scale tidal flats with an iterative approach on the waterline method, Estuar. Coast. Shelf Sci., 190, 11–22, https://doi.org/10.1016/j.ecss.2017.03.024, 2017.

Kang, Y., Lv, W., He, J., andDing, X.: Remote sensing of time-varying tidal flat topography, Jiangsu Coast, China, based on the waterline method and an artificial neural network model, Appl. ~~Proj. using microBRIAN image Process. Syst., 1989~~Sci., 10, https://doi.org/10.3390/app10103645, 2020.

Kerr, J. M. andPurkis, S.: An algorithm for optically-deriving water depth from multispectral imagery in coral reef landscapes in the absence of ground-truth data, Remote Sens. Environ., 210, 307–324, https://doi.org/10.1016/j.rse.2018.03.024, 2018.

Khan, M. J. U., Ansary, M. N., Durand, F., Testut, L., Ishaque, M., Calmant, S., Krien, Y., Saifu, A. K. M~~. and Papa~~., andPapa, F.: High-resolution intertidal topography from sentinel-2 multi-spectral imagery: Synergy between remote sensing and numerical modeling, Remote Sens., 11~~(24),~~, 1–20, https://doi~~:~~.org/10.3390/rs11242888, 2019.

Khojasteh, D., Hottinger~~Lee, Z., Franz, B., Shang, S., Dong, Q. and Arnone, R.: Some insights of spectral optimization in ocean color inversion, Remote Sens. Ocean. Sea Ice, Coast. Waters, Large Water Reg. 2011, 8175, 817508, doi:10.1117/12.897875, 2011.~~

, S., Felder, S., DeCesare, G., Heimhuber, V., Hanslow, D. J., andGlamore, W.: Estuarine tidal response to sea level rise: The significance of entrance restriction, Estuar. Coast. Shelf Sci., 244, 106941, https://doi.org/10.1016/j.ecss.2020.106941, 2020.

Formatted: Widow/Orphan control

Formatted: Widow/Orphan control

Khojasteh, D., Glamore, W., Heimhuber, V., andFelder, S.: Sea level rise impacts on estuarine dynamics: A review, Sci. Total Environ., 780, 146470, https://doi.org/10.1016/j.scitotenv.2021.146470, 2021.

Lee, Z., Carder, K. L., Mobley, C. D., Steward, R. G., andPatch, J. S.: Hyperspectral remote sensing for shallow waters I A semianalytical model, Appl. Opt., 37, 6329, https://doi.org/10.1364/ao.37.006329, 1998.

Li, F. K. andGoldstein, R. M.: Studies of Multibaseline Spaceborne Interferometric Synthetic Aperture Radars, IEEE Trans. Geosci. Remote Sens., 28, 88–97, https://doi.org/10.1109/36.45749, 1990.

Liu, Y., Li, M., Zhou, M., Yang, K~~. and Mao~~., andMao, L.: Quantitative analysis of the waterline method for topographical mapping of tidal flats: A case study in the dongsha sandbank, china, Remote Sens., 5~~(11),~~, 6138–6158, https://doi~~:~~.org/10.3390/rs5116138, 2013.

Formatted: Widow/Orphan control

Lorensen, W. E. ~~and Cline~~andCline, H. E.: Marching cubes: A high resolution 3D surface construction algorithm, Proc. 14th Annu. Conf. Comput. Graph. Interact. Tech. SIGGRAPH 1987, 21~~(4),~~, 163–169, https://doi~~:~~.org/10.1145/37401.37422, 1987.

Lyzenga, D. R.: Shallow-water bathymetry using combined lidar and passive multispectral scanner data, Int. J. Remote Sens., 6~~(1),~~, 115–125, https://doi~~:~~.org/10.1080/01431168508948428, 1985.

~~Lyzenga, D. R., Malinas, N. P. and Tanis, F. J.: Multispectral bathymetry using a simple physically based algorithm, IEEE Trans. Geosci. Remote Sens., 44(8), 2251–2259, doi:10.1109/TGRS.2006.872909, 2006.~~

~~Mason, D., Hill, D., Davenport, I., Flather, R. and Robinson, G.: Improving inter-tidal digital elevation models constructed by the waterline technique, Eur. Sp. Agency, (Special Publ. ESA SP, (414 PART 2), 1079–1082, 1997.~~

Mason, D. C. ~~and Davenport~~andDavenport, L. J.: Accurate and efficient determination of the shoreline in ERS-1 SAR images, IEEE Trans. Geosci. Remote Sens., 34~~(5),~~, 1243–1253, https://doi~~:~~.org/10.1109/36.536540, 1996.

Formatted: Widow/Orphan control

~~Mason, D. C., Davenport, I. J., Flather, R. A., Gurney, C., Robinson, G. J. and Smith, J. A.: A sensitivity analysis of the waterline method of constructing a digital elevation model for intertidal areas in ERS SAR scene of Eastern England, Estuar. Coast. Shelf Sci., 53(6), 759–778, doi:10.1006/ecss.2000.0789, 2001.~~

Mason, D. C., Scott, T. R~~. and Dance~~., andDance, S. L.: Remote sensing of intertidal morphological change in Morecambe Bay, U.K., between 1991 and 2007, Estuar. Coast. Shelf Sci., 87~~(3),~~, 487–496, https://doi~~:~~.org/10.1016/j.ecss.2010.01.015, 2010.

Formatted: Widow/Orphan control

McFeeters, S. K.: The use of the Normalized Difference Water Index (NDWI) in the delineation of open water features, Int. J. Remote Sens., 17~~(7),~~, 1425–1432, https://doi~~:~~.org/10.1080/01431169608948714, 1996.

Mohammadian, A., Morse, B., andRobert, J. L.: Calibration of a 3D hydrodynamic model for a hypertidal estuary with complex irregular bathymetry using adaptive parametrization of bottom roughness and eddy viscosity, Estuar. Coast. Shelf Sci., 265, 107655, https://doi.org/10.1016/j.ecss.2021.107655, 2022.

Morris, A. B. D., Coco, G., Bryan, K. R., Turner, I. L., Morris, B. D., Coco, G., Bryan, K. R., Turner, I. L., Street, K~~. and Vale~~., andVale, M.: Video-derived mapping of estuarine evolution Stable URL : https://www.jstor.org/stable/26481623 Linked references are available on JSTOR for this article : Video-derived mapping of estuarine evolution, ~~, (50),~~ 410–414, 2021.

Formatted: Widow/Orphan control

Murray, N. J., Phinn, S. R., DeWitt, M., Ferrari, R., Johnston, R., Lyons, M. B., Clinton, N., Thau, D~~. and Fuller~~., andFuller, R. A.: The global distribution and trajectory of tidal flats, Nature, 565~~(7738),~~, 222–225, https://doi~~:~~.org/10.1038/s41586-018-0805-8, 2019.

Nicholls, R. J. ~~and Cazenave~~andCazenave, A.: Sea-level rise and its impact on coastal zones, Science (80-.)., 328~~(5985),~~, 1517–1520, https://doi~~:~~.org/10.1126/science.1185782, 2010.

Nobuyuki Otsu: A Threshold Selection Method from Gray-Level Histograms, IEEE Trans. Syst. Man Cybern, 9~~(1),~~, 62–66, 1979.

Oppenheimer, M., Glavovic, B., Hinkel, J., van ~~de Wal~~deWal, R., Magnan, A. K., Abd-Elgawad, A., Cai, R., Cifuentes-Jara, M., DeConto, R. M., Ghosh, T., Hay, J., Isla, F., Marzeion, B., Meyssignac, B~~. and Sebesvari~~., andSebesvari, Z.: Sea Level Rise and Implications for Low Lying Islands, Coasts and Communities., IPCC Spec. Rep. Ocean Cryosph. a Chang. Clim., 355~~(6321),~~, 126–129, https://doi~~:~~.org/10.1126/science.aam6284, 2019.

Parodi, M. U., Giardino, A., ~~Van Dongeren~~VanDongeren, A., Pearson, S. G., Bricker, J. D~~. and Reniers~~., andReniers, A. J. H. M.: Uncertainties in coastal flood risk assessments in small island developing states, Nat. Hazards Earth Syst. Sci., 20~~(9),~~, 2397–2414, https://doi~~:~~.org/10.5194/nhess-20-2397-2020, 2020.

Pedrozo-Acuña, A., Ruiz de Alegria-Arzaburu, A., Mariño-Tapia, I., Enriquez, C~~. and González~~., andGonzález Villareal, F. J.: Factors controlling flooding at the Tonalá river mouth (Mexico), J. Flood Risk Manag., 5~~(3),~~, 226–244, https://doi~~:~~.org/10.1111/j.1753-318X.2012.01142.x, 2012.

~~Ryu, J. H., Won, J. S. and Min, K. D.: Waterline extraction from Landsat TM data in a tidal flat a case study in Gomso Bay, Korea, Remote Sens. Environ., 83(3), 442–456, doi:10.1016/S0034-4257(02)00059-7, 2002.~~

Rueda, A., Cagigal, L., Antolínez, J. A. A., Albuquerque, J. C., Castanedo, S., Coco, G., andMéndez, F. J.: Marine climate variability based on weather patterns for a complicated island setting: The New Zealand case, Int. J. Climatol., 39, 1777–1786, https://doi.org/10.1002/joc.5912, 2019.

Sagar, S., Roberts, D., Bala, B~~. and Lymburner~~., andLymburner, L.: Extracting the intertidal extent and topography of the Australian coastline from a 28 year time series of Landsat observations, Remote Sens. Environ., 195, 153–169, https://doi~~:~~.org/10.1016/j.rse.2017.04.009, 2017.

Salameh, E., Frappart, F., Marieu, V., Spodar, A., Parisot, J. P., Hanquiez, V., Turki, I., andLaignel, B.: Monitoring sea level and topography of coastal lagoons using satellite radar altimetry: The example of the Arcachon Bay in the Bay of Biscay, Remote Sens., 10, 1–22, https://doi.org/10.3390/rs10020297, 2018.

Salameh, E., Frappart, F., Almar, R., Baptista, P., Heygster, G., Lubac, B., Raucoules, D., Almeida, L. P., Bergsma, E. W. J., Capo, S., DeMichele, M. D., Idier, D., Li, Z., Marieu, V., Poupardin, A., Silva, P. A., Turki, I., andLaignel, B.: Monitoring Beach Topography and Nearshore Bathymetry Using Spaceborne Remote Sensing: A Review, Remote Sens., 11, https://doi.org/10.3390/rs11192212, 2019.

Formatted: Widow/Orphan control

Salameh, E., Frappart, F., Turki, I., andLaignel, B.: Intertidal topography mapping using the waterline method from Sentinel-1 & -2 images: The examples of Arcachon and Veys Bays in France, ISPRS J. Photogramm. Remote Sens., 163, 98–120, https://doi.org/10.1016/j.isprsjprs.2020.03.003, 2020.

Sobel, A. H., Camargo, S. J., Hall, T. M., Lee, C., Tippett, M. K~~. and Wing~~., andWing, A. a: Cyclone Intensity, Science (80-.).,, 353~~(6296),~~, 2016.

Spicer, P., Huguenard, K., Ross, L~~. and Rickard~~., andRickard, L. N.: High-Frequency Tide-Surge-River Interaction in Estuaries: Causes and Implications for Coastal Flooding, J. Geophys. Res. Ocean., 124~~(12),~~, 9517–9530, https://doi~~:~~.org/10.1029/2019JC015466, 2019.

Stephens, S. A., Bell, R. G., andHaigh, I. D.: Spatial and temporal analysis of extreme storm-tide and skew-surge events around the coastline of New Zealand, Nat. Hazards Earth Syst. Sci., 20, 783–796, https://doi.org/10.5194/nhess-20-783-2020, 2020.

Stewart, B.: Investigating groundwater derived nutrient fluxes within Tauranga harbour, New Zealand, 1994, 2021.

Stumpf, R. P., Holderied, K~~. and Sinclair~~., andSinclair, M.: Determination of water depth with high-resolution satellite imagery over variable bottom types, Limnol. Oceanogr., 48~~(1),~~, 547–556, https://doi.org/10.4319/lo.2003.48.1_part_2.0547, 2003.

Tay, H. W., Bryan, K. R., DeLange, W. P., andPilditch, C. A.: The hydrodynamics of the southern basin of Tauranga Harbour, New Zeal. J. Mar. Freshw. Res., 47, 249–274, https://doi.org/10.1080/00288330.2013.778300, 2013.

Traganos, D., Poursanidis, D., Aggarwal, B., Chrysoulakis, N., andReinartz, P.: Estimating satellite-derived bathymetry (SDB) with the Google Earth Engine and sentinel-2, Remote Sens., 10, https://doi.org/10.3390/rs10060859, 2018.

Turner, I. L., Harley, M. D., Almar, R., andBergsma, E. W. J.: Satellite optical imagery in Coastal Engineering, Coast. Eng., 167, 103919, https://doi.org/10.1016/j.coastaleng.2021.103919, 2021.

Vanhellemont, Q. andRuddick, K.: Atmospheric correction of metre-scale optical satellite data for inland and coastal water applications, Remote Sens. Environ., 216, 586–597, https://doi.org/10.1016/j.rse.2018.07.015, 2018.

Vos, K., Splinter, K. D., Harley, M. D., Simmons, J. A~~. and Turner~~., andTurner, I. L.: CoastSat: A Google Earth Engine-enabled Python toolkit to extract shorelines from publicly available satellite imagery, Environ. Model. Softw., 122, 104528, https://doi~~:~~.org/10.1016/j.envsoft.2019.104528, 2019.

Van ~~Der Walt~~DerWalt, S., Schönberger, J. L., Nunez-Iglesias, J., Boulogne, F., Warner, J. D., Yager, N., Gouillart, E~~. and Yu~~., andYu, T.: Scikit-image: Image processing in python, PeerJ, 2014~~(1),~~, 1–18, https://doi~~:~~.org/10.7717/peerj.453, 2014.

Wankang, Y., Baoshu, Y., Xingru, F., Dezhou, Y., Guandong, G~~. and Haiying~~., andHaiying, C.: The effect of nonlinear factors on tide-surge interaction: A case study of Typhoon Rammasun in Tieshan Bay, China, Estuar. Coast. Shelf Sci., 219~~(January),~~, 420–428, https://doi~~:~~.org/10.1016/j.ecss.2019.01.024, 2019.

Webster, P. J., Holland, G. J., Curry, J. A~~. and Chang~~., andChang, H. R.: Atmospheric science: Changes in tropical cyclone number, duration, and intensity in a warming environment, Science (80-.)., 309~~(5742),~~, 1844–1846, https://doi~~:~~.org/10.1126/science.1116448, 2005.

~~Wei, J., Wang, M., Lee, Z., Briceño, H. O., Yu, X., Jiang, L., Garcia, R., Wang, J. and Luis, K.: Shallow water bathymetry with multi-spectral satellite ocean color sensors: Leveraging temporal variation in image data, Remote Sens. Environ.,~~

Formatted: Widow/Orphan control

Formatted: Widow/Orphan control

Formatted: Widow/Orphan control

~~250(April), 112035, doi:10.1016/j.rse.2020.112035, 2020.~~
~~Zheng, P., Li, M., Wang, C., Wolf, J., Chen, X., De Dominicis, M., Yao, P. and Hu, Z.: Tide-Surge Interaction in the Pearl River Estuary: A Case Study of Typhoon Hato, Front. Mar. Sci., 7(April), 1–21, doi:10.3389/fmars.2020.00236, 2020.~~

Formatted: Don't adjust right indent when grid is defined, No widow/orphan control, Don't adjust space between Latin and Asian text, Don't adjust space between Asian text and numbers